공학박사 학위논문

Synthesis Design to Optimize the Active Site Formation for Oxygen Reduction Reaction in Fe-N-C Catalysts

철−질소−탄소 촉매 내 산소 환원 반응 활성점
형성의 최적화를 위한 합성 설계

2017 년 8 월

서울대학교 대학원

화학생물공학부

김 민 형

Abstract

Synthesis Design to Optimize the Active Site Formation for Oxygen Reduction Reaction in Fe-N-C Catalysts

Minhyoung Kim

School of Chemical and Biological Engineering

The Graduate School

Seoul National University

Polymer electrolyte fuel cells (PEFCs), which covert chemical energy of hydrogen and oxygen to electrical energy without any pollutant emission, have been received great attention as sustainable and clean energy conversion devices. Due to the sluggish oxygen reduction reaction (ORR) kinetics at the cathode side, Pt-based electrochemical catalysts have been commercially utilized in PEFC systems. However, excessive cost and scarcity of Pt hinder the economic feasibility of commercial PEFC devises. Therefore, various studies have been conducted for replacing Pt with cheap and abundant materials, such as heteroatom doped carbon, metal and nitrogen codoped carbon (M-N-C), metal chalcogenide, and metal oxide. Among those materials, Fe-N-C catalysts have shown the best performance with reaching the level

of Pt-based catalyst. These Fe-N-C catalysts are generally synthesized through the pyrolysis of a mixture of Fe, N and C precursors. Based on recent spectroscopic studies, the active site of these catalysts are proposed to have Fe-N_4 coordination structure within the micropores of carbon matrix. However, there are no established guideline or general strategy yet for Fe-N-C catalyst synthesis with optimizing the Fe-N_4 active site formation. In this thesis, I investigated the precursor and carbon support effect on Fe-N-C catalyst synthesis with systematic experiments, and suggested the rational synthesis design for optimizing the Fe-N_4 ORR active sites.

In the precursor study, the Fe-N coordination precursor effect on the active site formation was investigated. To clarify this effect, three phenanthroline isomers were used as N precursor, because only 1,10-phenanthroline forms coordination bonds with Fe and other two phenanthrolines doesn't form these bonds. I found that these coordination bonds suppressed the gasification of phenathroline precursor during high temperature pyrolysis, while it was completely gasified without Fe-N coordination. This suppression of precursor gasification due to coordination bonds resulted in an even distribution of Fe without particle aggregation. During heat treatment, furthermore, the Fe-N coordination helped N to be located in the pyridinic N position, which is more favorable for active site formation than other N positions. Due to the above effects, Fe-N-C catalysts derived from 1,10-phenanthroline precursor showed much superior ORR activity compared to catalysts from other phenanthrolines. This results suggest that the utilization of Fe-N coordinated precursors can be a good strategy to design an optimized Fe-N-C catalysts with increasing the possibility of Fe-

N_4 active site formation.

In carbon support study, the role of pre-defined microporosity of carbon supports in ORR catalytic site formation was investigated. The microporosity of the carbon supports are initially controlled by using hot CO_2 treatment. Then, Fe and N are doped into these supports by precursor impregnation and subsequent pyrolysis. In the synthesized Fe–N–C catalysts, the more developed microporosity in the parent carbon supports facilitates more iron and nitrogen contents, especially pyridinic nitrogen, and Fe–N–Cs derived from carbon supports with higher microporosities show enhanced ORR activity, strongly suggesting that a high catalytic site density can be achieved by utilizing carbon supports with well-developed microporosities. This results indicate that development of microporosity of carbon supports can be another strategy to get highly active Fe-N-C catalysts with enlarging the Fe-N_4 active site density.

Keywords: Oxygen reduction reaction, non-precious metal catalyst, Fe-N-C catalyst, active site formation, coordination state, pore structure, microporosity

Student Number: 2013-30983

Contents

List of Tables

List of Figures

x

Chapter 1. Introduction

1.1 Fuel Cells

Fuel cell is an energy conversion devise that converts chemical energy from a fuel into electrical energy through an electrochemical reaction [1]. Fuel cells, in some aspect, have characteristics in common with combustion engines and batteries. [2, 3]. Like batteries, fuel cells generate electricity directly from chemical energy without moving part. So, they are far more efficient, silent and highly reliable compared to combustion engines. Also, fuel cell only produce water as byproduct without emission of undesirable pollutant, such as NO_x, SO_x, etc. Like combustion engines, on the other hand, fuel cell requires an external sources of fuel and oxygen or air to continue the chemical reaction, whereas batteries only hold a closed store of chemical energy in them. This make fuel cells can produce electricity continuously as long as the fuels are supplied. Lastly, fuel cells allows easy independent scaling between power and capacity, providing the opportunity for many applications. Due to many advantages as mentioned above, fuel cells have received great attention as future energy sources.

1.1.1 Principle of Fuel Cell

Fuel cells combine fuel (such as hydrogen and alcohols) and oxidant (oxygen) to produce electricity [4]. The basic principle of the fuel cells is illustrated in **Fig. 1.1**. The unit cell of fuel cells consists of an electrolyte and two electrodes; anode and cathode. The most basic fuel cell is a hydrogen fuel cell, and the following reactions take place at each side of electrode in hydrogen fuel cell:

Anode:	$2H_2$	$\rightarrow$ $4H^+ + 4e^-$	$E^0 = 0.000$ V
Cathode:	$O_2 + 4H^+ + 4e^-$	$\rightarrow$ $2H_2O$	$E^0 = 1.229$ V
Overall:	$O_2 + 2H_2$	$\rightarrow$ $2H_2O$	$E_{cell} = 1.229$ V
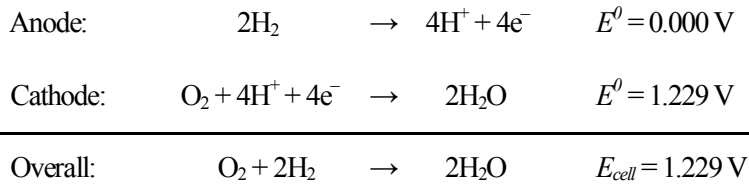
When a hydrogen fuel cell is operated, hydrogen is oxidized at the anode side, while oxygen is reduced at the cathode side. While electrons from cathode side are moved to the anode side through the external circuit, produced protons at the anode side are transferred to the cathode side through the electrolyte, completing the closed circuit. The theoretical open circuit voltage of a hydrogen fuel cell is 1.229 V at 298 K. In practice, however, it is around 1 V at open circuit due to hydrogen crossover and/or internal current. When current density is increased, moreover, cell voltage is decreased by the overpotential from charge transfer resistance, ohmic resistance and mass transfer resistance [5]. Under practical load condition, the cell voltage of hydrogen fuel cell is generally between 0.5 V and 0.8 V.
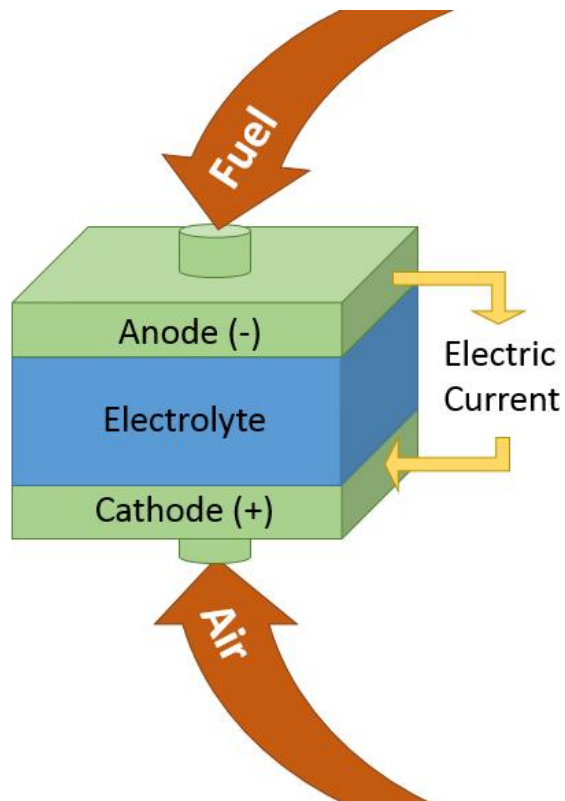
Figure 1.1. Schematic illustration for basic principle of fuel cell.

1.1.2 Types of Fuel Cells

Since the first description of the fuel cell principle by Sir William Grove in 1939, different types of fuel cells have been developed [6]. These fuel cells differ in the electrolytes and electrodes materials used, the fuels used and their operating temperature, etc. Depending on the working temperature, the main types of fuel cells are categorized into three groups; the low-temperature / the medium-temperature / high-temperature fuel cells [7]. The "alkaline fuel cell" (AFC), the "proton exchange membrane fuel cell" (PEMFC), the "anion exchange membrane fuel cell" (AEMFC) and the "direct methanol fuel cell" (DMFC) are low-temperature fuel cells, and the "phosphoric acid fuel cell" (PAFC) is medium-temperature fuel cell, and the "molten carbonate fuel cell" (MCFC) and the "solid oxide fuel cell" (SOFC) are high-temperature fuel cells. These fuel cells are named according to the electrolyte used; except DMFC, which is labeled by the fuel used. Detailed features of different fuel cell types are shown in **Table 1**.

Table 1. Fuel cell types and features

Type	Electrolyte	Charge carrier	Fuel	Operating temp. (°C)	Applications
PEMFC	Polymer membrane	H^+	H_2	40 - 90	Transportation Portable power Distributed generation
AEMFC	Polymer membrane	OH^-	H_2	40 - 90	Portable power
DMFC	Polymer membrane	H^+	CH_3OH	60 - 120	Portable power
AFC	Liquid KOH (immobilized)	OH^-	H_2	90 - 100	Military Space
PAFC	Liquid H_3PO_4 (immobilized)	H^+	H_2	150 - 200	Distributed generation
MCFC	Molten carbonate	CO_3^{2-}	H_2, CH_4	600 - 700	Distributed generation
SOFC	Ceramic	O^{2-}	H_2, CH_4, CO	700 - 1000	Auxiliary power Distributed generation

1.2. Polymer Electrolyte Fuel Cells (PEFCs)

Polymer electrolyte fuel cells (PEFCs), which have three subclasses of the "proton exchange membrane fuel cell" (PEMFC), the "anion exchange membrane fuel cell" (AEMFC) and the "direct methanol fuel cell" (DMFC), are a type of fuel cell using ion conducting polymer as their electrolyte. The general structure and operation of PEFC is illustrated in **Fig. 1.2**. During PEFC operation, hydrogen gas and oxygen gas (air) are supplied to anode and cathode, respectively. Through the electrochemical reactions, supplied hydrogen and oxygen are combined to water with producing electricity.

PEFCs have superior characteristics to other fuel cell classes. At first, PEFCs currently exhibit the highest power density among all the fuel cell types. Also, they can provide good start-stop capability. Furthermore, their operating temperature (~ 80°C) is relatively low compared to the others [8]. From these advantages, PEMCs have been received great attention in many applications, especially transport applications. Indeed, numerous automobile companies, such as GM, Toyota, Nissan, and Hyundai-Kia motor, have recently conducted active researches on PEFC because it is one of the most suitable power sources for replacing internal combustion engine in vehicle [9, 10]. Moreover, US Department of energy (DOE) encourages PEFC research [11], and various national research institutes, such as Los Alamos, Argon, and Lawrence

Berkeley National Laboratory also participate in development of PEFC technologies [12-18].
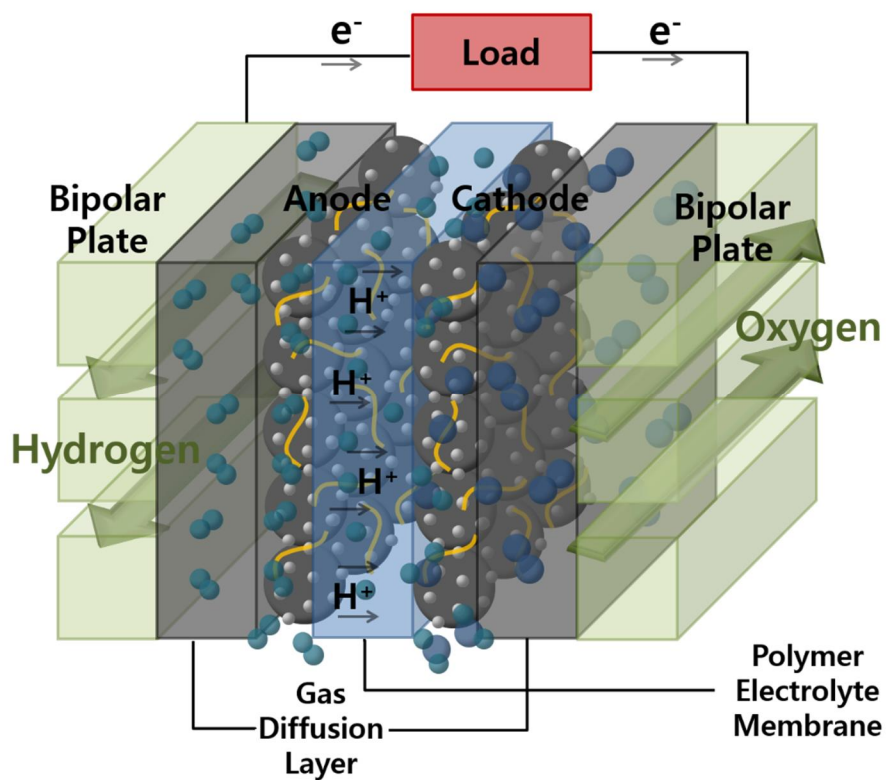
Figure 1.2. Illustration of PEFC operation.

1.2.1. Components of PEFC

In PEFC single cell, the anode and the cathode are separated by the polymer electrolyte membrane (PEM). This PEM conducts protons from the anode to the cathode. For the minimizing ohmic losses from the PEM, the membrane should be thin enough. At the same time, however, the PEM should also guarantee the electronic isolation, mechanical stability and impermeability of reactant gases [19]. Therefore, only perfluorosufuric acid membranes, such as Nafion membrane (Dupont), have been commercially used at present time. The PEM is sandwiched between two gas diffusion electrodes (GDEs), which consist of at least two layers: catalyst layers and gas diffusion layers. Often these two layers are separated by a microporous layer [20]. The catalyst layer typically consists of carbon supported Pt nano-particle electocatalysts [21]. The gas diffusion layer usually consists of a porous carbon paper or carbon cloth, which can transport the reactants and electrons at the same time. GDEs should have optimum porosity, good electric and thermal conductivity, chemical and mechanical stability. Also, the optimum hydrophobicity is needed in order to avoid water flooding problem [22].

The combination of PEM and the sandwich of GDEs is called a membrane electrode assembly (MEA). Typically, several MEAs are connected in series, separated by

bipolar plates, and the array of MEAs is generally called a stack [23]. This fuel cell stack is completed by endplates. The PEFC single cell components mentioned above are systemically visualized in **Fig. 1.3**.
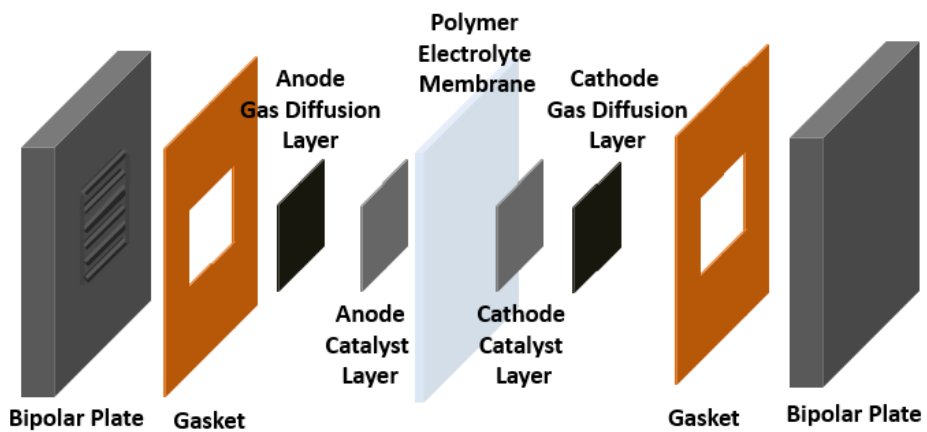
Figure 1.3. The components and structure of PEFC single cell.

1.2.2 Overpotentials in PEFC

In PEFCs, the hydrogen is oxidized at the anode and the oxygen is reduced at the cathode, and a theoretically predicted voltage from Gibbs free energy is 1.229 V. During PEFC operation, however, the real voltage output for a fuel cell is much smaller than theoretical voltage due to overpotentials [5]. These overpotentials influence the shape of i-V curve of PEFC, which can visualize the overall fuel cell performance. There are three major types of overpotentials, which gives a i-V curve its typical S-shape characteristics. Each of these overpotentials is associated with following fuel cell steps:

1. Activation overpotentials (voltage losses from the electrochemical reactions)
2. Ohmic overpotentials (voltage losses from the charge carrier conductions)
3. Concentration overpotentials (voltage losses from the mass transport)

The output fuel cell voltage can be expressed by subtracting all the overpotentials from a thermodynamically predicted fuel cell voltage.

$$V = E_0 - \eta_{act} - \eta_{ohmic} - \eta_{conc}$$

Where, V is the real output voltage of fuel cell, E_0 is thermodynamically predicted voltage, η_{act} is activation overpotentials, η_{ohmic} is ohmic overpotentials and η_{conc} is concentration overpotentials. In the fuel cell *i*-V curve, as shown in **Fig. 1.4**, the activation overpotentials mostly affect in the low current density region, and the ohmic overpotentials are most marked in the middle range of the curve, and the concentration overpotentials most intense in high current density region.

While the ohmic and concentration overpotentials can be handled with improved electrolyte membranes and advanced electrode structure designs, the activation overpotentials provide a particular challenge because the kinetics of the electrochemical reaction in fuel cell is governed by the catalyst materials. In PEFC, compared to the anode side with fast hydrogen oxidation reaction kinetics, the cathode suffers from sluggish oxygen reduction reaction (ORR) kinetics [24], limiting the PEFC performance with high activation overpotential. In this respect, ORR reaction have been considered as one of the most important parts in PEFC operation.
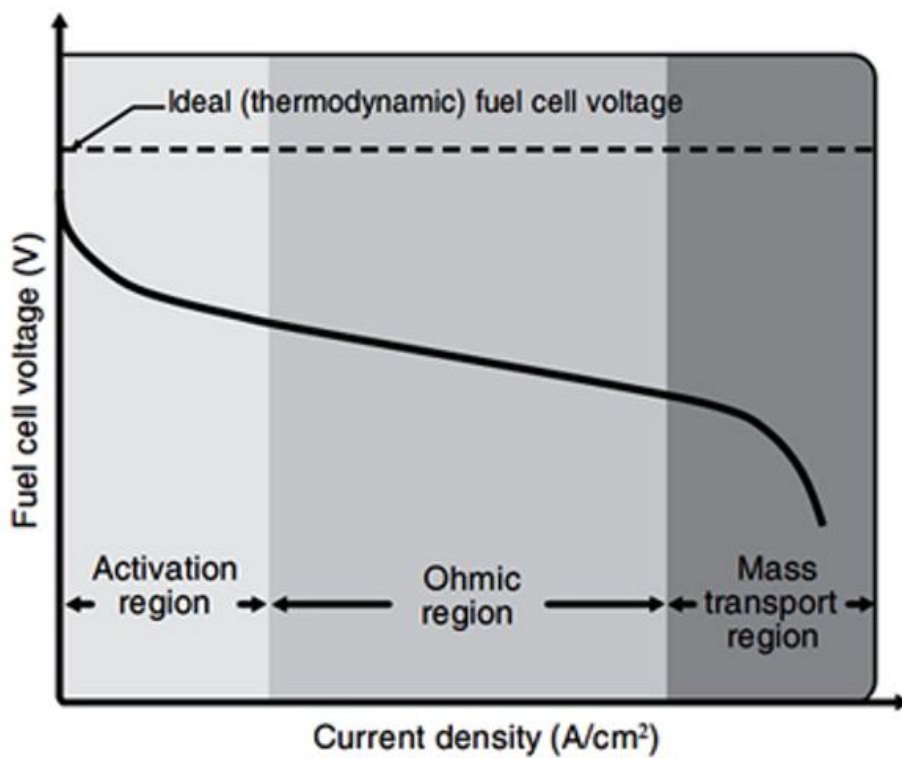
Figure 1.4. Schematic of fuel cell *i*-V curve and three major overpotentials. (Adapted from O'hayre, Ryan, et al. Fuel cell fundamentals. John Wiley & Sons, 2016)

1.2.3 Catalysts for Oxygen Reduction Reaction (ORR)

As mentioned earlier, in PEFC, ORR kinetics is very slow. For a practical usable level in PEFC, a cathode ORR catalyst is essential to speed up the ORR kinetics. At the current PEFC technology status, Pt nanoparticle catalysts supported on carbon materials are practically used as cathode catalysts. Due to their limited availability and high cost, however, these Pt catalysts are not the viable for PEFC mass production and commercialization [25]. Therefore, two different approaches have been taken in developing the inexpensive and highly active PEFC catalyst materials. The first approach is to increase Pt utilization in the catalyst layers. This approach can be accomplished by alloying Pt with inexpensive metal, such as Fe, Co, Ni, etc [26-28]. In this way, the amount of expensive Pt used would be minimized with lowering the catalyst price. However, Pt-based catalysts still suffer from long-term stability [29, 30]. The limited reserves of Pt also remaining problem for large-scale applications of PEFCs [25]. Clearly, the first approach mentioned above cannot be a long-term solution and a more economical and sustainable approach will be required. In this context, recent approach is to replace Pt-based catalysts with non-precious metal-based electrocatalyst materials, and many researchers have explored alternative non-precious metal-based electrocatalysts, such as such as heteroatom doped carbon [31-34], metal and nitrogen codoped carbon (M-N-C) [35-38], metal chalcogenide [39-42], and metal oxide [43-46]. Among these candidates, Fe–N–C catalysts have shown promising ORR activities

approaching those of commercial Pt-based catalysts [14].

1.3 Fe-N-C ORR Catalysts

Research into the ORR using Fe–N–C electrocatalysts started with Jasinski in 1964, who reported that metal–phthalocyanine showed ORR activity in alkaline media [47]. In the 1970s, enhanced ORR activities and stabilities were demonstrated by electrocatalysts obtained from the pyrolysis of Fe–N_4 and Co–N_4 (Fe and Co ions coordinated with four nitrogens) macrocycles supported on carbon surfaces under an inert atmosphere [48]. After Yeager discovered that the macrocycles could be substituted by simple metal salts and N-rich polymers [49], Fe–N–C catalysts have been readily produced by high-temperature pyrolysis of a mixture of individual Fe, N, and C precursors.

1.3.1 Synthesis Approaches of Fe-N-C Catalysts

There are many options to combine Fe, N, and C elements to form a Fe-N-C catalyst precursor (**Fig. 1.5**) and this precursor composite undergoes one or several heat treatments for Fe-N-C catalyst synthesis. The various synthesis approaches have been invented, and these can be categorized as follows:

1. The supported macrocycle approach (pyrolysis of macrocycle/carbon) [50-52]

2. Templating method (pore and morphology control with sacrificial template) [53-55]

3. Foaming agent approach (pore generation with using thermally decomposable precursor) [56, 57]

4. N-molecule or Fe-ligand approach (pyrolysis of Fe and N molecule precursor after impregnated into carbon support pores) [58-61]

5. N-polymer approach (pyrolysis of Fe, N and C compound after polymerization of N-containing monomer) [38, 62-64]

6. Gaseous N-precursor approach (pyrolysis of Fe, C compound under NH_3 or CH_3CN condition) [65-68]

7. Thermally decomposable metal-organic frameworks (MOF) approach (pyrolysis of Fe-based MOF or Zn-based MOF after impregnation of Fe precursors) [36, 69-71]

The resulting ORR activity and performance of such catalysts from different synthetic routes vary by orders of magnitude, because of the different coordination chemistry of the formed catalytic sites and variable active site density in resultant catalysts.
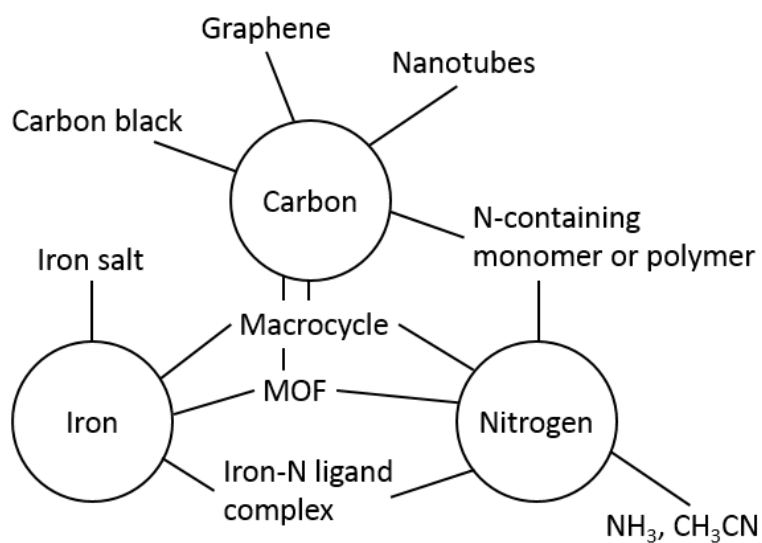
Figure 1.5. Different types of precursors for the iron, nitrogen, and carbon.

1.3.2 Nature of Active Sites in Fe-N-C Catalysts

There have been numerous studies to figure out where are the ORR active sites in Fe-N-C catalysts. Various tools, such as time of flight secondary-ion mass-spectroscopy (ToF-SIMS), X-ray absorption spectroscopy (XAS), Mössbauer spectroscopy, X-ray photoelectron spectroscopy (XPS), X-ray diffraction (XRD) or transmission electron microscopy (TEM), have been applied to investigate Fe-N-C catalysts [72-83]. At first, studies with ToF-SIMS revealed the existence of Fe species on the outmost surface of Fe-N-C catalysts even after several acid washing steps, demonstrating that the coordination of Fe by N atoms is strong enough to protect from dissolution in acid [73]. ToF-SIMS studies also reveal that Fe is at the center of the most ORR-active site with confirming the similar trend relation between signal intensity of FeN_4-like species and ORR activity [80]. With XAS study, on the other hand, the local geometric and electronic structures around Fe atoms in Fe-N-C catalysts can be investigated. According to X-ray absorption near-edge structure (XANES) analysis (**Fig. 1.6a**), pyrolysis at high temperature resulted in the loss of the 7117 eV pre-peak, which is the characteristic peak for the D_{4h} symmetry of square-planar structure of iron(III) tetraphenyl porphyrin (FeTPP) [75, 81]. The extended X-ray absorption fine structure (EXAFS) analysis (**Fig. 1.6b**) also demonstrated the significant structural changes (from square-planar to square-pyramidal) started at around 500 °C, as suggested by the disappearance of the FT-EXAFS peaks between 2 and 3 Å [75]. The

Mössbauer spectroscopy studies on the Fe-N-C catalysts also revealed that the nature of active sites have D3 square-pyramidal structure (micropore-hosted $Fe(II)N_4$ species with high spin) [77]. In the D3 site, as shown in **Fig 1.7**, a Fe atom is located at the center of four pyridinic-N functionalities on the edge of carbon, but out of the plane consisting of those N atoms. This D3 content showed a similar trend to ORR activity, identifying the D3 site is responsible for high ORR activity in Fe-N-C catalysts (**Fig 1.8**) [77].
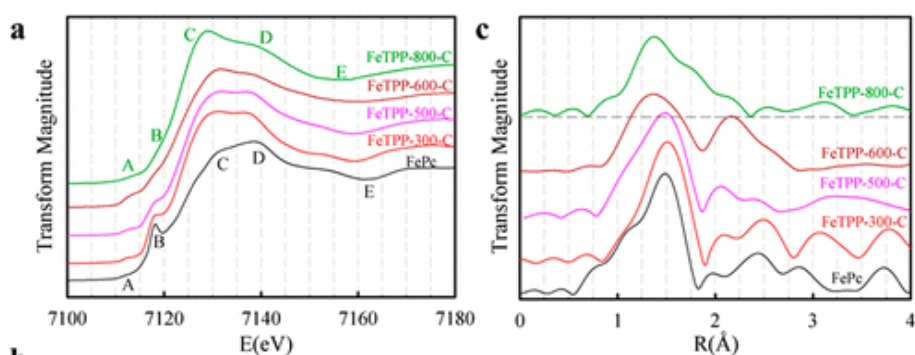
Figure 1.6. The evidences of Fe displacement during pyrolysis: (a) XANES spectra of FeTPP-pyrolyzed catalysts and reference Fe(II) phthalocyanine. (b) Corresponding EXAFs spectra. (Adapted from Jia, Qingying, et al. ACS nano 2015, 9, 12496)
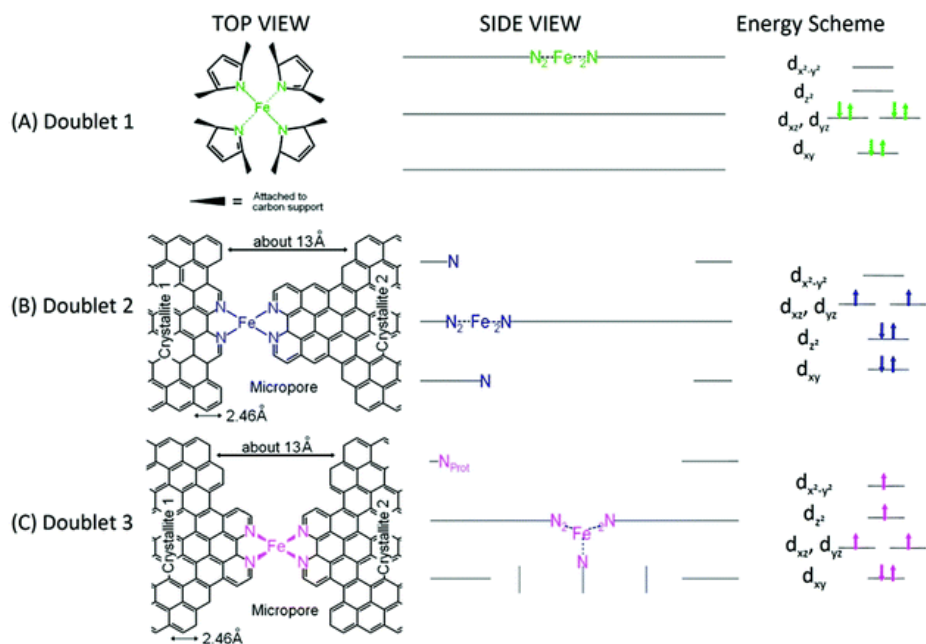
Figure 1.7. Proposed Fe-N$_4$ structures from the Mössbauer spectroscopy:
(a - c) Top and side views of proposed structure for Mössbauer doublet D1, D2 and D3.
(Adapted from Kramm, Ulrike I., et al. Phys. Chem. Chem. Phys., 2012, 14, 11673)
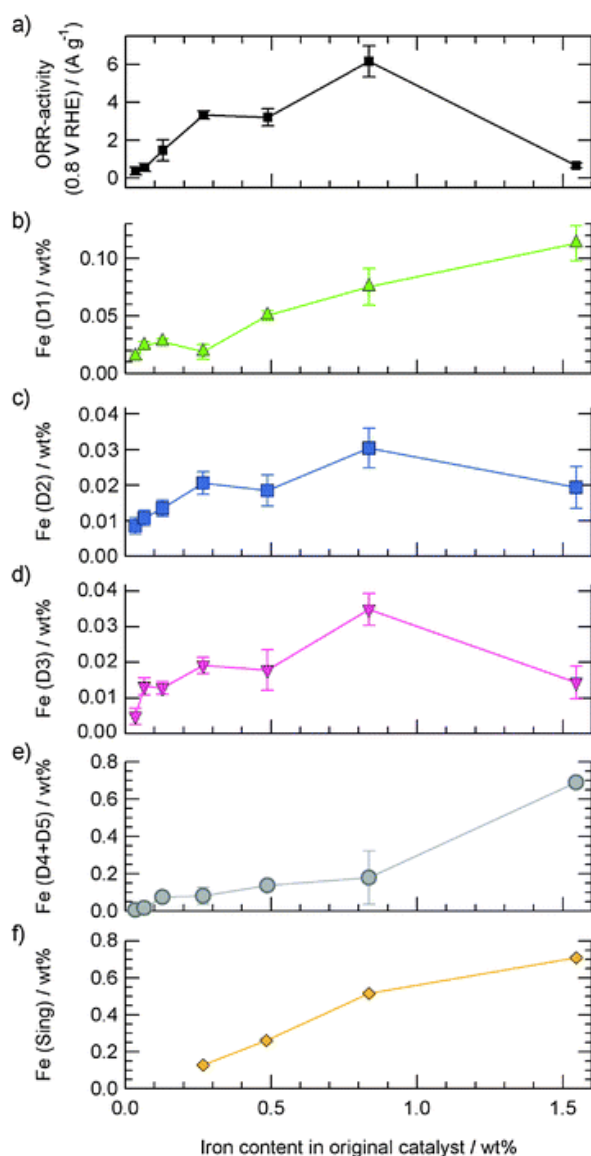
Figure 1.8. Compared evolution of the ORR activity and the relative composition of each Fe species: (a) ORR activity versus nominal iron content and (b - f) content of each Fe species detected by Mössbauer spectroscopy against the nominal iron content. (Adapted from Kramm, Ulrike I., et al. Phys. Chem. Chem. Phys., 2012, 14, 11673)

1.3.3 Challenges in Fe-N-C Catalyst Synthesis

As mentioned in 1.3.2, the ORR active site consists of FeN_{2+2} structure hosted in micropores, which means Fe is atomically distributed and coordinated to four N atoms in an ideal Fe-N-C catalyst. However, a variety of Fe related crystalline phases (such as Fe, Fe oxide, Fe carbide, Fe nitride, etc.) are formed during this pyrolysis step in real, because high temperature treatment is essential for Fe-N-C catalyst synthesis (see section 1.3.1). Although some of those phases are ORR active, their activities are much smaller than that of FeN_{2+2} site [84-86]. Furthermore, these Fe crystalline particles block the active FeN_{2+2} site when ORR reaction occurs. This means most crystalline Fe phases formed during synthesis are unwanted residue in the resultant Fe-N-C catalysts. Therefore, acid leaching post treatment has been generally conducted for removing these unwanted Fe residues [84, 86], and consequently only small amount of Fe could be involved in ORR, which means the low active site density of acid-leached Fe-N-C catalysts. Therefore, the active site densities of Fe-N-C catalysts in current status are generally about one order magnitude lower than that of state-of-the-art 47wt% Pt/C catalysts (active site density of 3.2×10^{20} sites cm^{-3}) [26]. The low active site density of Fe-N-C catalysts require more catalyst loading for practical performance level of PEFC operation, resulting in additional mass transport problem with thicker catalyst layers [37]. Obviously, therefore, maximizing the catalytic site density in Fe-N-C catalysts is important. However, if the amount of Fe precursor was increased for

maximizing the active site density, particle aggregation of Fe would become severe during heat treatment at high temperature, rather than forming the ideal FeN_{2+2} active site. In order to solve this dilemma, rational synthesis design for Fe-N-C catalyst synthesis is needed at this stage.

1.4 Subjects of This Thesis

In this thesis, the main theme is how to synthesize the optimal Fe-N-C catalysts with maximizing the FeN_{2+2} active site in resultant catalysts. There are two different approaches; (1) precursor study (the effect of Fe and N precursor coordination state on active site formation in Fe-N-C catalysts), (2) carbon support study (The role of pre-defined microporosity of carbon support in catalytic site formation in Fe-N-C catalysts).

1.4.1 Precursor Study

As mentioned in 1.3.2, the active sites of Fe–N–C catalysts have been proposed to consist of a central Fe ion coordinated to four pyridinic-Ns attached to two edges of the graphitic carbon surface (FeN_{2+2} structure) [77]. Thus, it can be suggested that the initial presence of Fe-N coordination bonds in precursor state is helpful for forming the FeN_{2+2} structure. Recently, Dodelet and coworkers demonstrated the coordination chemistry of precursor compounds could affect the ORR activity of resultant Fe-N-C catalysts after pyrolysis [87]. They suggested the optimized catalysts could be obtained from the precursor with Fe-ligand coordination by its helping the localization of Fe on the surface of ZIF-8 support. Several other papers also reported the Fe-N-C catalysts with high ORR activity by using the N-coordinated Fe precursors [87-94], and some of

those papers suggested that homogeneous Fe distribution from chemically mixed precursor states with Fe-N coordination bonds was the main reason for the better performance of their catalysts [91, 92]. For the rational synthesis design, however, more deep investigation is needed to verify how the precursor coordination state affects the Fe-N$_4$ active site formation during high-temperature pyrolysis. In this work, I suggest a systematic approach to determining the distinct precursor coordination effect on forming the catalytic sites of Fe-N-C catalysts.

1.4.2 Carbon Support Study

As mentioned in 1.3.2, the active sites of Fe–N–C catalysts are known to be hosted in micropores of the catalysts [77]. Recently, Lefèvre and coworkers demonstrated the direct correlation between the microporous surface area (pore diameter < 2 nm) and ORR activity in Fe–N–C catalysts [74, 95]. After that, significantly enhanced performances have been reported after impregnation of an iron precursor and pore filler (PF) into microporous carbon supports and subsequent two-step pyrolysis in Ar and NH$_3$ gases [35,36]. Thus, the development of accessible micropores bearing Fe–N$_{2+2}$ catalytic sites in Fe–N–C catalysts is essential for achieving greatly enhanced ORR activity. Considering that carbon supports usually act as main frameworks in Fe–N–C catalysts during and after the synthetic process, the micropore structure within the initial carbon supports of Fe–N–C catalysts could be a crucial factor in active site

formation. With this in mind, carbon support materials with high microporosity, such as Ketjenblack [96], Black Pearls 2000 [35], and ZIF-8 [36], have been utilized to maximize active site density. However, to my knowledge, no study has shown that the pre-defined microporosity of parent carbon supports plays a distinct role in forming Fe–N_{2+2} active sites, determining the catalytic site density and, ultimately, the ORR activities of the electrocatalysts. In this study, I present an effective approach for verifying the distinct role of pre-defined microporosity in carbon supports, which is directly related to the formation of catalytic sites within the accessible micropores of Fe–N–C catalysts.

Chapter 2. Experimental

2.1 Precursor Study

2.1.1 Chemicals and Materials

Fe^{II}acetate, phenanthrene, 1,7-phenanthroline (1,7-phen), 4,7-phenanthroline (4,7-phen) and 1,10-phenanthroline (1,10-phen) were purchased from Aldrich. All chemicals were used as received. Ketjenblack EC-600JD (KB) was purchased from Akzo Nobel Polymer Chemicals. The KB powders were pretreated in aqueous HCl solution for 12 h at 80 °C to remove possible metal impurities. Nafion perfluorinated resin solution (Nafion, 5 wt% in lower aliphatic alcohol and water) and carbon supported platinum (Pt, HiSpec 3000, 20 wt%) was received from Aldrich and Alfa Aesar, respectively.

2.1.2 Precursor Variation and Preparation of Fe-N-C Catalysts

As shown in Fig. 2.1., four different precursor groups were prepared for this study. Each group has common Fe precursor of Fe^{II}acetate, but has different pore fillers. 1,7-phen, 4,7-phen, 1,10-phen were used as pore fillers and N precursors. Phenanthrene

was used as an N free pore filler for control sample synthesis, and denoted as 0,0-phen for convenience in this study.

Catalyst samples were synthesized by impregnation of precursors into pretreated KB carbon support and subsequent pyrolysis of mixture powders. Precursor solutions were prepared by mixing Fe precursor with pore-filler in ethyl alcohol. After 15 min of ultrasonication, each precursor solution was impregnated into dry KB powders via repeated dropping and mixing with an agate mortar. After drying in an electric oven for overnight, all the resultant powder samples were heated to 800 °C at a heating rate of 5 °C min^{-1} under an Ar atmosphere and maintained at that temperature for 1 h. The final products were denoted as Fe/pore filler name/KB, such as Fe/0,0-phen/KB, Fe/1,7-phen/KB, Fe/4,7-phen/KB, and Fe/1,10-phen/KB. Fe free samples were prepared with same procedure except the absence of Fe precursor in the precursor solutions. These samples were denoted as pore filler name/KB.
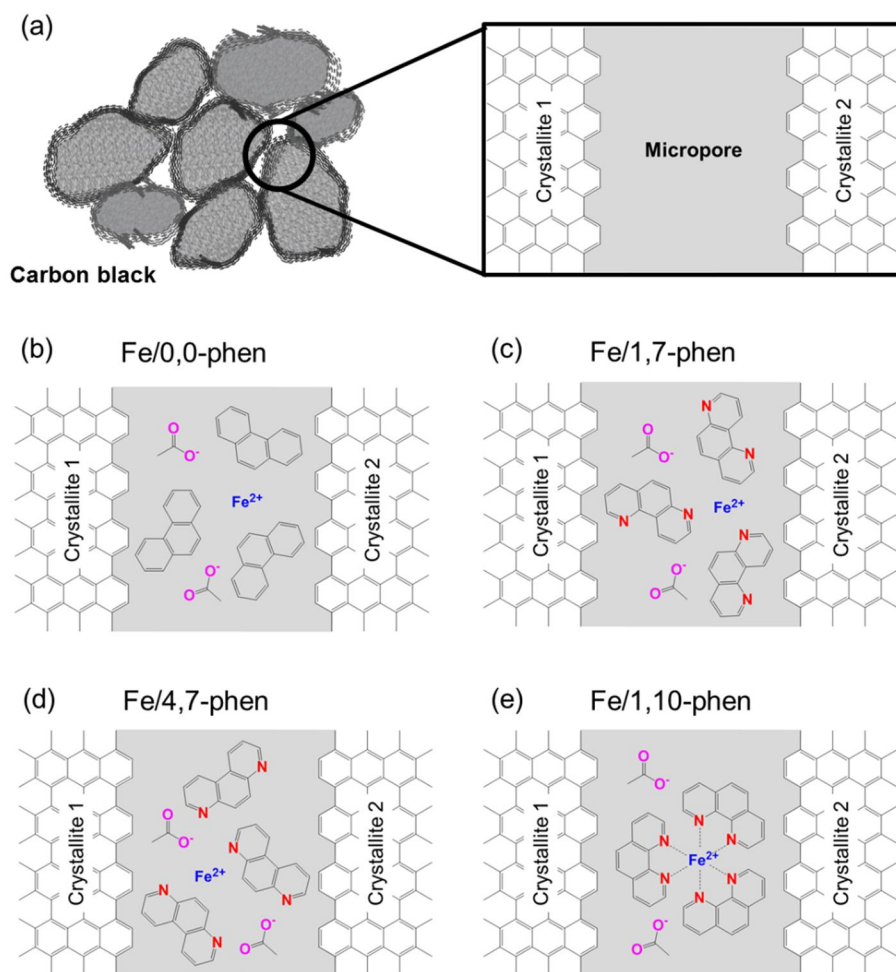
Figure 2.1. Schematic images of carbon micropores impregnated with different precursor compositions: (a) carbon black and its empty micropores. Carbon microcpores impregnated with (b) Fe/0,0-phen (c) Fe/1,7-phen, (d) Fe/4,7-phen and (e) Fe/1,10-phen.

2.1.3 Material Characterizations

For precursor characterizations, UV/Vis absorbance spectra of precursor solutions (6 mg Fe^{II}acetate, 40 mg phenanthrolines in 5 mL ethyl alcohol) were obtained with Beckman DU 650 spectrophotometer. After rotary evaporation of above solutions, the weight-loss of dried precursor compounds during heat treatment by thermogravimetric analysis (TGA) using TA Instruments SDT Q600.

For resultant catalyst samples, Transmission electron microscopy (TEM) and Energy-filtered TEM (EFTEM) images were recorded using a FEI Tecnai F-20 microscopes and a JEOL-2200FS equipped with an image Cs corrector, respectively. X-ray diffraction (XRD) experiments were conducted with a Rigaku D/MAX 2500 using Cu Ka radiation (λ=0.15406 nm). High-resolution X-ray photoelectron spectroscopy (XPS) data were obtained at the 8A2 beamline in the Pohang Accelerator Laboratory (PAL), equipped with a Scienta SES100 electron analyzer. Fe K-edge X-ray absorption spectroscopy (XAS) was performed at the 8C beamline in the PAL. Elemental analysis and inductively coupled plasma atomic emission spectroscopy (ICP-AES) were conducted using a CE Instrument Flash 2000 elemental analyzer and a Perkin Elmer Optima 4300DV spectrometer, respectively.

2.1.4 Electrochemical Measurements

All electrochemical experiments were conducted with an Autolab potentiostat (PGSTAT) using a conventional three-electrode cell. Platinum wire and saturated Ag/AgCl were used as the counter and reference electrode, respectively. A catalyst-coated rotating disk electrode (RDE, Pine Research Instrumentation) was used as the working electrode. To prepare the catalyst ink, catalyst samples were mixed with deionized water, Nafion solution (5 wt % in isopropanol, Aldrich), and 2-propanol by ultrasonication. The catalyst ink was deposited on a glassy carbon electrode (5.0 mm diameter) of the RDE, with catalyst loading of 0.4 mg cm^{-2} (20 μg_{Pt} cm^{-2} for the benchmark Pt/C catalyst; 20 wt% Pt/C, Johnson Matthey). 0.1 M KOH and 0.5 M H$_2$SO$_4$ aqueous solutions were used as alkaline and acid electrolyte, respectively. The solution temperature was kept at 20 °C with a water jacket. The reference electrode was calibrated with respect to the reversible hydrogen electrode (RHE) before the experiments, by determining the hydrogen oxidation and evolution potential with a Pt working electrode in H$_2$-saturated solutions. For cleaning the catalysts, potential pre-cycling was performed between 0.05 and 1.15 V (vs RHE) for 30 cycles at a scan rate of 50 mV s^{-1} in an Ar-saturated electrolytes. After that, RDE test was performed at 1600 rpm with a scan rate of 10 mV s^{-1} in an O$_2$-saturated electrolyte. In order to remove the non-Faradaic term from RDE measurements, the double layer capacity current recorded under same condition in an Ar-saturated electrolyte was subtracted.

The apparent electron transfer numbers were estimated from RDE data at 400, 900, 1200, and 1600 rpm at 0.60 V (vs. RHE) using the Koutecky-Levich (K–L) equation:

$$\frac{1}{j} = \frac{1}{j_L} + \frac{1}{j_K} = \frac{1}{B\omega^{1/2}} + \frac{1}{j_K} \tag{1}$$

$$B = 0.62nFC_0(D_{O_2})^{2/3}\upsilon^{-1/6} \tag{2}$$

where, j, j_L, and j_K are the measured, diffusion limiting, and kinetic current densities, respectively, ω is the electrode rotation speed, F is the Faraday constant (96,485 C mol^{-1}), C_0 is the saturated O_2 concentration in bulk solution (1.21×10^{-6} mol cm^{-3}), D_{O_2} is the diffusion coefficient of O_2 (1.86×10^{-5} cm^2 s^{-1}), and υ is the kinetic viscosity of the electrolyte (0.01 cm^2 s^{-1}). As a kinetic parameter, the kinetic current density was calculated at 0.85 V (vs. RHE) from the mass transfer correction of the RDE measurements using the following equation:

$$j_K = \frac{j \times j_L}{(j_L - j)} \tag{3}$$

The accelerated durability test (ADT) was conducted using the Department of Energy (DOE) protocol, in which the potential was cycled between 0.6 V and 1.0 V (vs. RHE) 10,000 times at a scan rate of 50 mV s^{-1} in Ar-saturated electrolyte.

2.2 Carbon support study

2.2.1 Chemical and Materials

Resorcinol (Junsei), formaldehyde (Amresco), ammonia solution (28%, Wako), Fe^{II} acetate (Aldrich) and 1,10-phenanthroline (Aldirich) were used without purification. Nafion perfluorinated resin solution (Nafion, 5 wt% in lower aliphatic alcohol and water) and carbon supported platinum (Pt, HiSpec 3000, 20 wt%) was received from Aldrich and Alfa Aesar, respectively.

2.2.2 Preparation of Carbon Supports

For the resorcinol–formaldehyde polymer (RFP), resorcinol (0.76 g) and formaldehyde (0.88 g) were mixed in a solution of ammonia (28% aq.) in deionized water (200 mL). After stirring for 24 h at room temperature, the reaction mixture was placed in an oven and heated for 24 h at 90 °C without stirring. The solid product was recovered by centrifugation and washed several times with deionized water. For the carbonization process, RF polymer spheres were heated from ambient temperature to 800 °C under a N_2 atmosphere over 3 h at a heating rate of 4.3 °C min^{-1}. The carbonized powders were denoted as RFC. For the porosity control, carbon dioxide activation was performed on the as-prepared RFC powders. RFC powders were placed in an alumina boat in a quartz tube in the isothermal zone of a tubular furnace and purged with a N_2 flow. The samples were heated to 900 °C at a heating rate of

30 °C min^{-1} under N$_2$ flow. Then, the flowing gas was changed to CO$_2$ (1000 mL min^{-1}) and the activation conditions were maintained for different time periods (30, 120 and 240 min). After the programmed activation times, the gas flux was changed back to nitrogen during the cooling process. The activated carbon samples were denoted as RFC_CX, where X is the CO$_2$ activation time.

2.2.3 Preparation of Fe-N-C Catalysts

The Fe-N-doped porous carbon spheres were produced by impregnation of the Fe and N precursor into activated carbon and subsequent pyrolysis of these mixtures. First, the precursor solution was prepared by mixing Fe^{II}acetate (234 mg), 1,10-phenanthroline (800 mg), and ethyl alcohol (10 mL). Then, 0.6 mL of the precursor solution was added to each carbon sample (250 mg) via repeated dropping and mixing with a mortar. The sample mixtures were dried in an electric oven (75 °C) for 12 h. The resulting powder samples were pyrolyzed at 800 °C (heating rate, 5 °C min^{-1}) for 1 h under a N$_2$ flow. The resultant carbon materials were washed with 0.5 M H$_2$SO$_4$ at 80 °C for 8 h to remove excess Fe species. After filtering with deionized water several times and drying in the oven for 12 h, the carbon samples were again heated under the same conditions as the previous pyrolysis step. The final products were denoted as Fe-N-RFC_CX. The overall synthetic process of Fe-N-RFC_CXs was shown in **Fig. 2.2.**
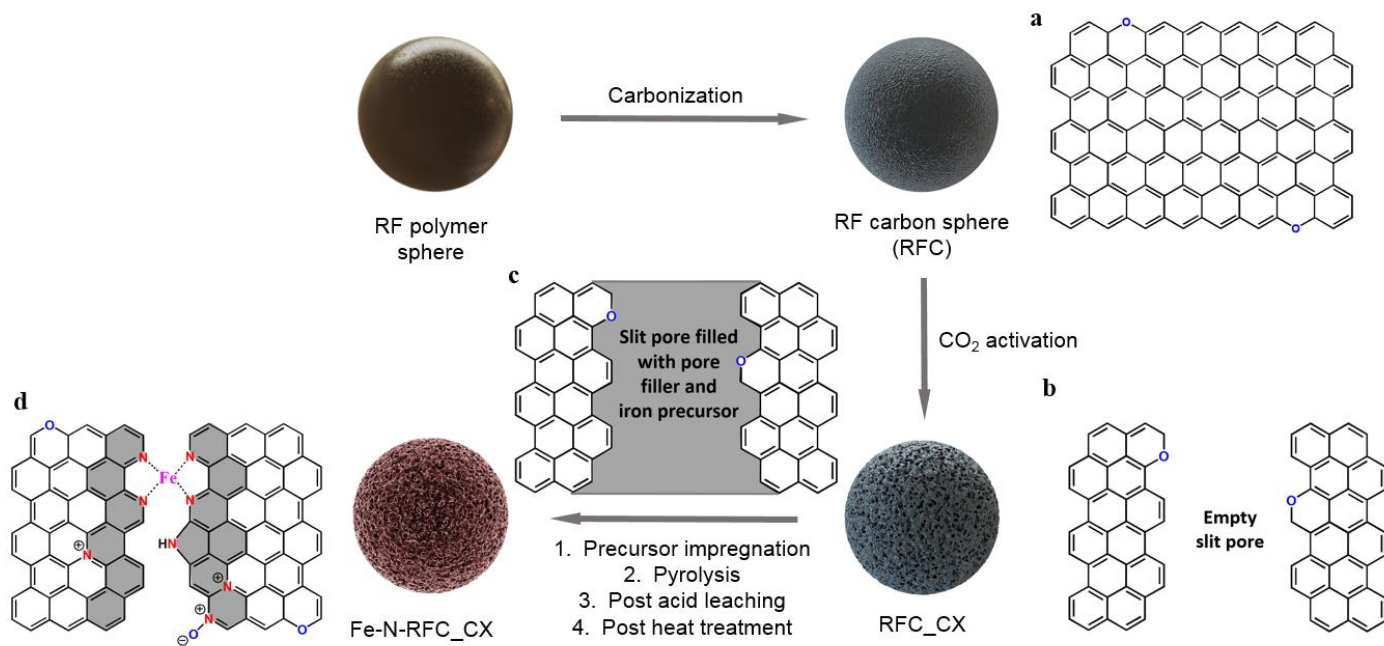
Figure 2.2. Illustration of the synthesis of Fe-N-RFC_CX (X: CO₂ activation time): (a) Plan view of a graphite surfaces before activation. (b) Plan view of an empty slit pore between two graphite edge surfaces after activation. (c) Plan view of a slit pore filled with pore filer and iron precursor after impregnation. (d) Plan view of the presumed Fe and N configuration after Fe and N doping process. Shaded region comes from pore filler.

2.2.4 Material Characterizations

Scanning electron microscopy (SEM) and transmission electron microscopy (TEM) images were recorded using HITACHI S-4800 and FEI Tecnai F-20 microscopes, respectively. Energy-filtered TEM (EFTEM) were conducted using a JEOL-2200FS equipped with an image Cs corrector. X-ray diffraction (XRD) data were obtained on a Rigaku D/MAX 2500 using Cu Kα radiation ($\lambda = 0.15406$ nm). High-resolution X-ray photoelectron spectroscopy (XPS) experiments were conducted at the 8A2 beamline in Pohang Accelerator Laboratory, equipped with a Scienta SES100 electron analyzer. Nitrogen sorption isotherms were measured at –196 ℃ on a BEL MAX adsorption volumetric analyzer. Inductively coupled plasma atomic emission spectroscopy (ICP-AES) and elemental analysis data were obtained using a Perkin Elmer Optima 4300DV spectrometer and CE Instrument Flash 2000 elemental analyzer, respectively.

2.2.5 Electrochemical Measurements

The catalyst ink was prepared by mixing catalyst samples with deionized water, Nafion solution (5 wt%), and 2-propanol with ultrasonication. This catalyst ink was deposited on a glassy carbon electrode (5.0-mm diameter) in a rotating disk electrode (RDE) and dried at room temperature. The catalyst loadings were 0.5 mg cm^{-2} (20 μg_{Pt} cm^{-2} for commercial Pt/C catalyst; Johnson Matthey, 20 wt% Pt/C). All

electrochemical measurements in this study were conducted in a conventional three-electrode cell using an Autolab potentiostat (PGSTAT) with platinum wire, saturated Ag/AgCl, and the catalyst-coated RDE as the counter, reference, and working electrodes, respectively. The electrolyte was 0.1 M KOH and 0.5 M H_2SO_4 aqueous solution and the temperature was kept at 20 °C using a water jacket. All potentials in this study refer to the reversible hydrogen electrode (RHE), which was determined by a calibration measurement using the platinum wire as the working electrode in each H_2-saturated solution. Cyclic voltammetry (CV) was performed between 0.05 and 1.10 V (vs. RHE) with a scan rate of 50 mV s^{-1}. The RDE test was measured in O_2-saturated electrolyte at 1600 rpm with a scan rate of 5 mV s^{-1}. In order to remove the double layer capacity term, the current recorded in Ar-saturated electrolyte under the same scan conditions was subtracted. The limiting currents and half-wave potentials were determined at 0.30 V (vs. RHE) and half the limiting current from the ORR curves, respectively. The apparent electron transfer numbers were estimated from RDE data with 400, 900, 1200, and 1600 rpm at 0.60 V (vs. RHE) using the Koutecky-Levich (K–L) equation:

$$\frac{1}{j} = \frac{1}{j_L} + \frac{1}{j_K} = \frac{1}{B\omega^{1/2}} + \frac{1}{j_K} \tag{1}$$

$$B = 0.62nFC_0(D_{O_2})^{2/3}\upsilon^{-1/6} \tag{2}$$

where, j, j_L, and j_K are the measured, diffusion limiting, and kinetic current

densities, respectively, ω is the electrode rotation speed, F is the Faraday constant (96,485 C mol^{-1}), C_0 is the saturated O_2 concentration in bulk solution (1.21×10^{-6} mol cm^{-3}), D_{O_2} is the diffusion coefficient of O_2 (1.86×10^{-5} cm^2 s^{-1}), and v is the kinetic viscosity of the electrolyte (0.01 cm^2 s^{-1}). As a kinetic parameter, the kinetic current density was calculated at 0.85 V (vs. RHE) from the mass transfer correction of the RDE measurements using the following equation:

$$j_K = \frac{j \times j_L}{(j_L - j)} \tag{3}$$

The methanol tolerance test was performed with chronoamperometry at a constant voltage of 0.7 V (vs. RHE). Methanol was injected into the electrolyte after 400 s, adjusting the final methanol concentration to 1 M. Output currents were normalized to those under the initial state. The accelerated durability test (ADT) was conducted using the Department of Energy (DOE) protocol, in which the potential was cycled between 0.6 V and 1.0 V (vs. RHE) 10,000 times at a scan rate of 50 mV s^{-1} in Ar-saturated electrolyte.

Chapter 3. Results and Discussion

3.1 Precursor Study

3.1.1 Precursor: Coordination State

The coordination states of each precursor group were investigated by UV/Vis absorbance spectra of precursor solutions. As shown in **Fig. 3.1a**, the absorption peak at 510 nm of $[Fe^{II}(phen)^3]$ were only observed in the UV/Vis spectrum of Fe/1,10-phen, corresponding the reddish color of Fe/1,10-phen solution (**Fig. 3.1b**) [87,97,98]. This indicates that only Fe/1,10-phen precursor group was impregnated into carbon pores with Fe-phenanthroline coordination complex form, whereas other precursor groups impregnated with physically mixed compound form in the absence of chelation, as shown in **Fig. 2.1.**

In order to investigate the pyrolysis behavior of each precursor group during heat treatment, thermogravimetric analysis (TGA) of dried precursor compounds was conducted under inert gas atmosphere. The pyrolysis progresses of each precursor compound are shown in the TGA curves (**Fig. 3.2a**). For Fe/1,7-phen and Fe/4,7-phen compounds, most of their weight was gasified at a temperature below 300 ℃, and only about 5 % of initial weight was remained at 800 ℃. In the case of Fe/1,10-phen/KB, on the other hand, over 40 % of the initial weight was remained at that temperature. Considering that pure 1,10-phen was completely gasified below 300 ℃

(**Fig. 3.2b**), the coordination state of Fe/1,10-phen compound significantly suppressed

gasification of precursor during pyrolysis.
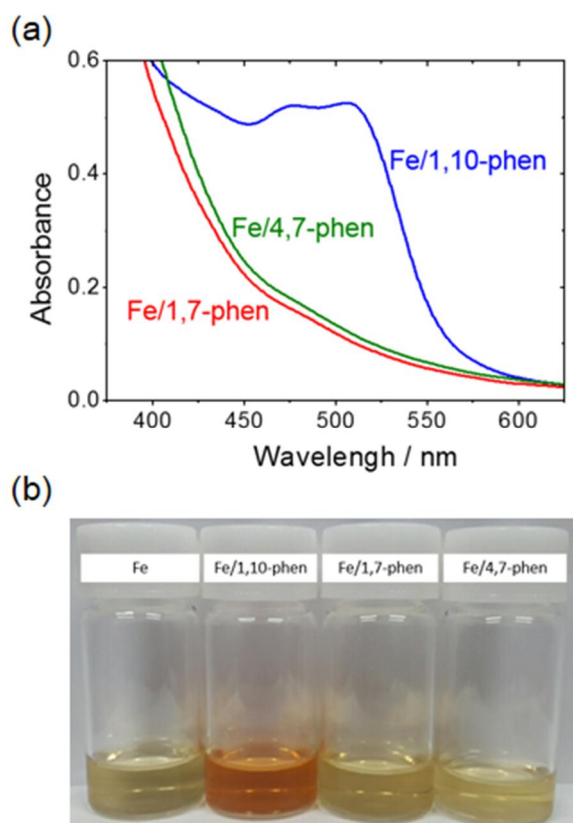
Figure 3.1. The coordination state of each precursor group: (a) UV/Vis spectra for Fe/pore filler precursors, and (b) digital camera images for Fe and Fe/pore filler solutions.
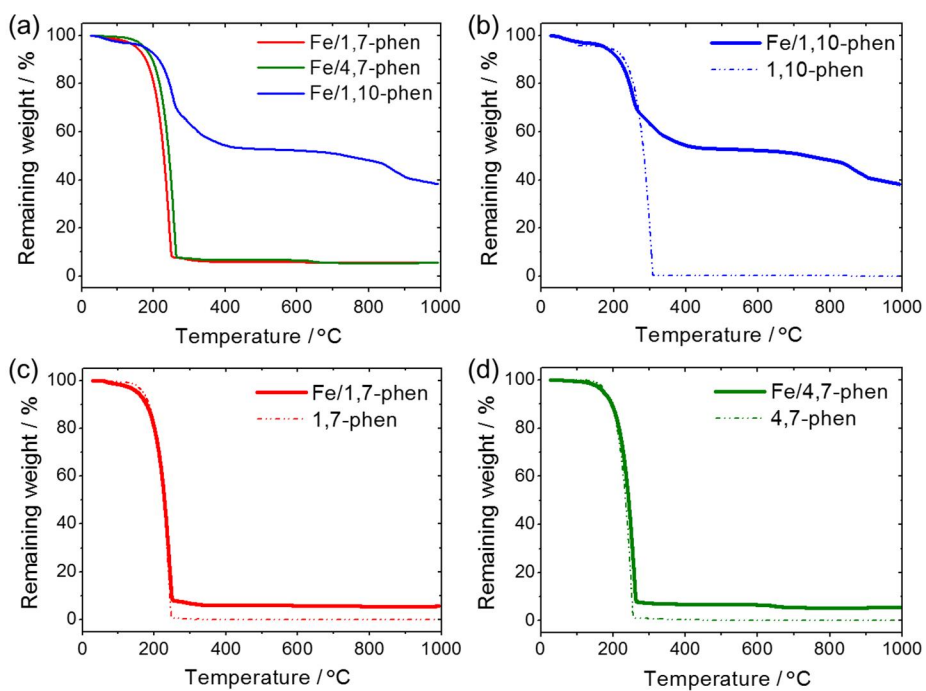
Figure 3.2. Thermal behaviors of each precursor group: (a) TGA curves for Fe/pore filler precursors, and comparative TGA curves of pore fillers with/without Fe for (b) 1,10-phen, (c) 1,7-phen and (d) 4,7-phen.

3.1.2 Physicochemical Characterizations of Fe-N-C Catalysts

After precursor impregnation, the obtained powder samples were subjected to high-temperature pyrolysis at 800 °C. With the same amount of impregnated precursor, however, resultant N contents of Fe/1,7-phen/KB and Fe/4,7-phen/KB were much lower than that of Fe/1,10-phen/KB (**Table 2**). The N content of Fe-N-C catalysts is known as one of the crucial factor for ORR activity [60, 66, 67]. Therefore, in an attempt to verify the pure precursor coordination effect, the amounts of impregnated phen precursors were controlled for adjusting the resultant N contents in all samples to about 0.45 wt%. The Fe contents were also adjusted to about 0.7 wt% in all the catalysts. Further characterizations and ORR measurements were conducted with these N-content-controlled samples (**Table 3**). After synthesis, the XRD pattern of the Fe/1,10-phen/KB catalyst showed only carbon-related peaks, whereas the Fe/0,0-phen/KB, Fe/1,7-phen/KB, and Fe/4,7-phen/KB showed additional peaks, corresponding to Fe_3O_4 (**Fig. 3.3**). The TEM images (**Fig. 3.4**) also showed that no particle aggregation was observed in Fe/1,10-phen/KB catalyst while several particles were found in Fe/1,7-phen/KB and Fe/4,7-phen/KB samples. In order to examine the elemental distributions in catalyst samples, electron energy loss spectroscopy (EELS) analysis was conducted with EFTEM, and resultant elemental mapping images of each catalyst were shown in **Fig. 3.5**. In Fe/1,7-phen/KB and Fe/4,7-phen/KB samples, Fe only existed in aggregated particles while N was embedded evenly throughout the

catalysts. On the other hand, both Fe and N were homogeneously distributed in Fe/1,10-phen/KB, indicating that Fe species were well dispersed in this catalyst without any particle aggregation even after high-temperature heat treatment. These results clearly suggest that Fe/1,10-phen coordination complex facilitate the uniform Fe distribution, suppressing the aggregation of Fe-based particle during high temperature pyrolysis.

Further investigation on the local and electronic structure of Fe species in Fe/pore filler/KB catalyst samples was conducted with XAS analysis. **Fig. 3.6** showed Fe K-edge XANES spectra of catalysts and reference samples, and each spectrum possessed the characteristic features labeled as A-E. The XANES spectra of Fe/0,0-phen/KB, Fe/1,7-phen/KB, and Fe/4,7-phen/KB had similar features (A-E) to the Fe_3O_4 spectrum, which was consistent the their XRD patterns (**Fig. 3.3**). On the other hand, the XANES spectrum of Fe/1,10-phen/KB was compared with that of Fe phthalocyanine (FePc) for estimating its Fe-N_x structure. Recently, Mukergee and their co-workers demonstrated that the XANES spectra of their pyrolyzed catalysts showed increased intensity of features C and decreased intensities of features B and D compared to that of FePc [75]. These trends suggested that the pyrolyzed catalysts had central Fe located out of N_4-plane by the distortion of the D_{4h} symmetric Fe-N_4 structure of FePc [75, 81]. In this study, Fe/1,10-phen/KB also showed similar spectrum features with reported Fe-N-C catalysts, determining its nonplanar Fe-N_4 structure.

The EXAFS Fourier transforms spectra also revealed the local structure differences between Fe/1,10-phen/KB and others (**Fig. 3.7**). The EXAFS spectra of Fe/0,0-phen/KB, Fe/1,7-phen/KB, and Fe/4,7-phen/KB showed two distinct peaks: one peak at around 1.5 Å and the other peak between 2.5 and 3.0 Å. Matching with two peaks of the reference spectra of Fe_2O_3/Fe_3O_4 [99], the former one was assigned to the Fe-O bond distance and latter one was attributed to the Fe-Fe interaction in Fe oxide. In contrast to above samples, the EXAFS spectrum of Fe/1,10-phen/KB showed only one dominant peak at around 1.5 Å assigned to Fe-N(O) shell, and minor signal around 2.2 Å from Fe-Fe back scattering demonstrated the minimized Fe-Fe bonds were formed in it compared to the others [100].

XPS analysis was also conducted to examine the effect of precursor coordination on N configuration after high temperature pyrolysis. High-resolution N1s spectra of pore filler/KB and Fe/pore filler/KB samples (**Fig. 3.8**) were deconvoluted into three nitrogen peaks: pyridinic N (approx. 398.6 eV), pyrrolic N (approx. 399.9 eV) and graphitic N (approx. 401.2 eV). For the pore filler/KB samples, all the samples shows similar N peak configurations regardless of pore filler species (**Fig. 3.8a** and **Table 3**). With Fe addition, no noticeable change was observed in Fe/1,7-phen/KB and Fe/4,7-phen/KB samples (**Fig. 3.8b** and **Table 3**), indicating that physical mixing of those pore fillers with Fe had negligible effect on N doping site in carbon matrix during heat treatment. In Fe/1,10-phen/KB, however, the relative portion of graphitic N peak was

significantly decreased compared to other samples (**Fig. 3.8b** and **Table 3**), implying

that Fe-N coordination selectively suppressed N doping at graphitic site.

Table 2. N contents of each catalyst with different amount of impregnated phenanthroline precursor.

Precursor group	Fe/1,7-phen/KB		
Phenanthroline [mg]	40	80	120
N content [wt%]	0.28	0.39	0.46

Precursor group	Fe/4,7-phen/KB		
Phenanthroline [mg]	40	80	120
N content [wt%]	0.36	0.47	0.50

Precursor group	Fe/1,10-phen/KB		
Phenanthroline [mg]	10	20	40
N content [wt%]	0.45	0.83	1.36

Fe^{II} acetate : 6 mg, ethyl alcohol : 1 mL, Ketjenblack : 200 mg

Table 3. Physical and chemical properties of pore filler/KB, Fe/pore filler/KB catalysts.

Sample	Fe-ICP (wt%)	N-EA (wt%)	relative percentage of different N functionalities (%)			Half-wave potential (V vs. RHE)	ORR onset potential (V vs. RHE)
			pyridinic	graphitic	pyrrolic		
0,0-phen/KB	-	-	-	-	-	0.66	0.77
1,7-phen/KB	-	0.55	56.9	31.7	11.4	0.67	0.85
4,7-phen/KB	-	0.56	57.0	31.9	11.1	0.68	0.86
1,10-phen/KB	-	0.55	56.7	32.0	11.3	0.68	0.86
Fe/0,0-phen/KB	0.71	-	-	-	-	0.63	0.77
Fe/1,7-phen/KB	0.72	0.45	59.1	28.5	12.4	0.74	0.89
Fe/4,7-phen/KB	0.72	0.46	57.8	28.6	13.6	0.74	0.90
Fe/1,10-phen/KB	0.71	0.45	65.6	15.0	19.4	0.87	1.00
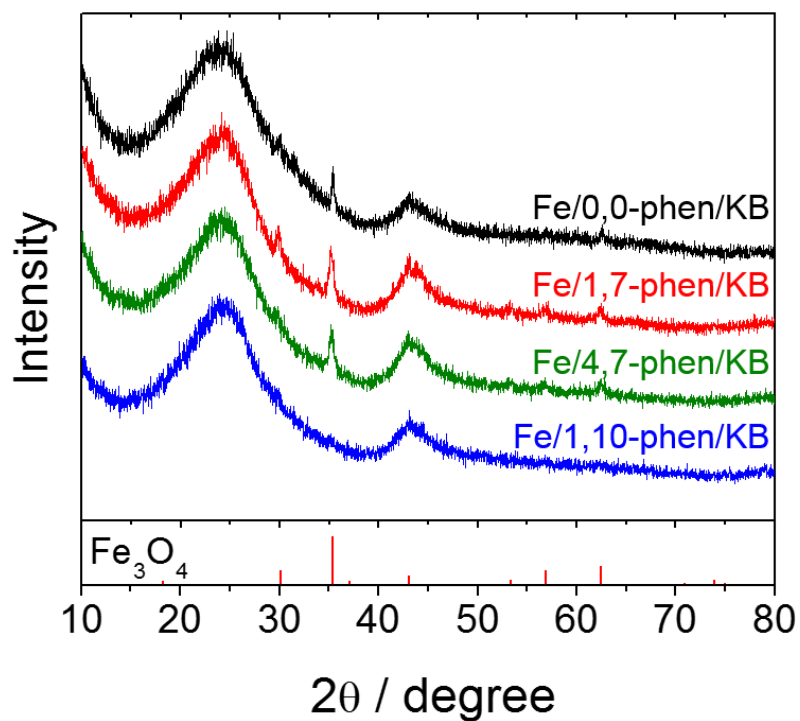
Figure 3.3. XRD patterns of Fe/pore filler/KB catalysts.
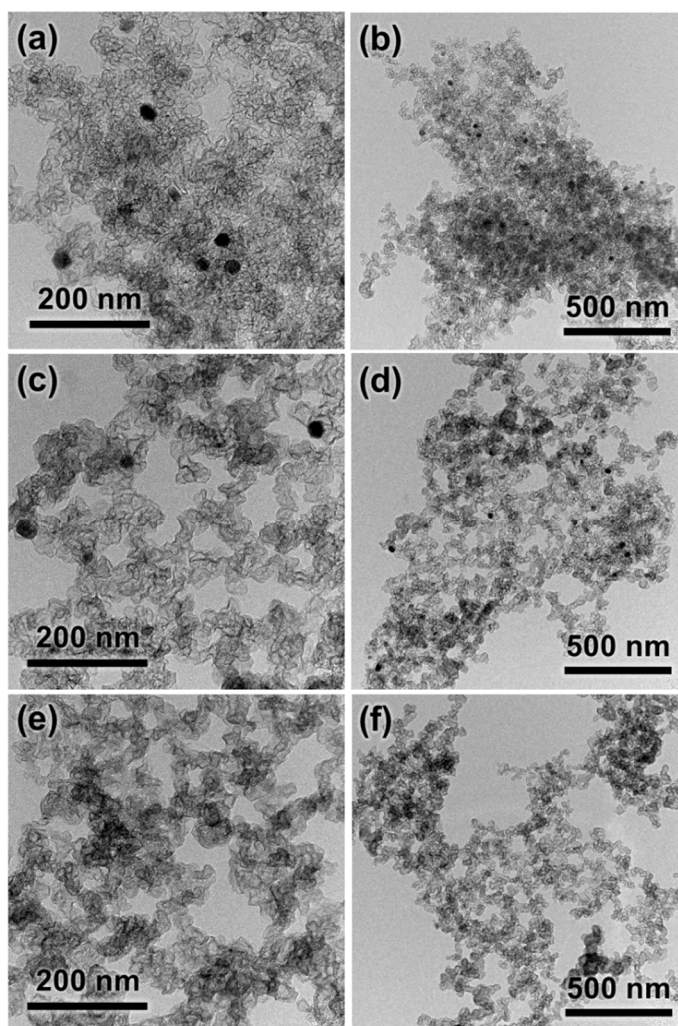
Figure 3.4. TEM images of Fe/pore filler/KB catalysts: (a, b) Fe/1,7-phen/KB, (c, d) Fe/4,7-phen/KB and (e, f) Fe/1,10-phen/KB.
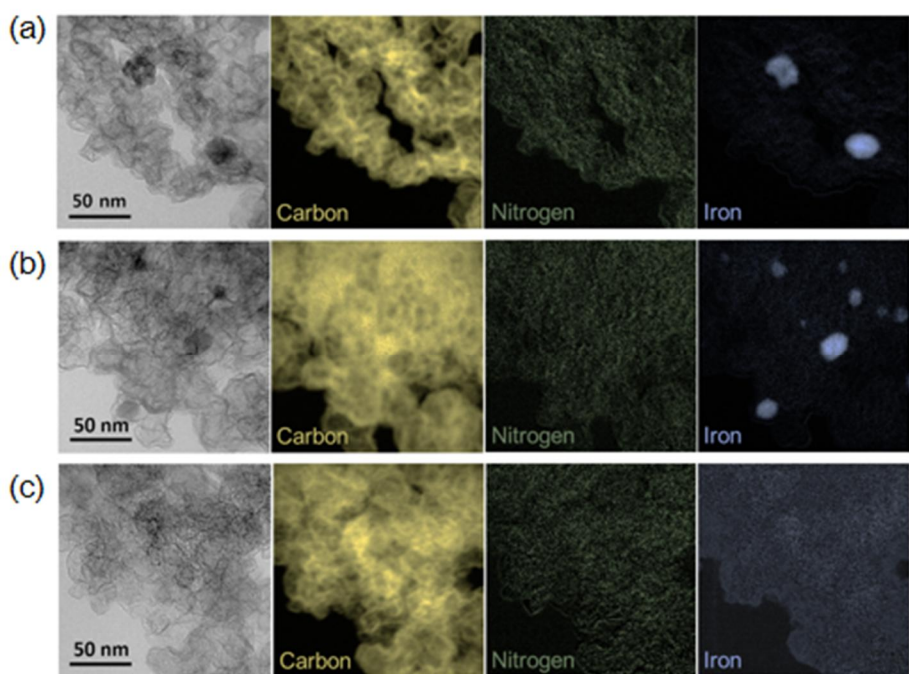
Figure 3.5. Energy-filtered TEM elemental mapping images of Fe/pore filler/KB catalysts: Sequence of the unfiltered images and carbon, nitrogen and iron elemental maps of (a) Fe/1,7-phen/KB, (b) Fe/4,7-phen/KB and (c) Fe/1,10-phen/KB.
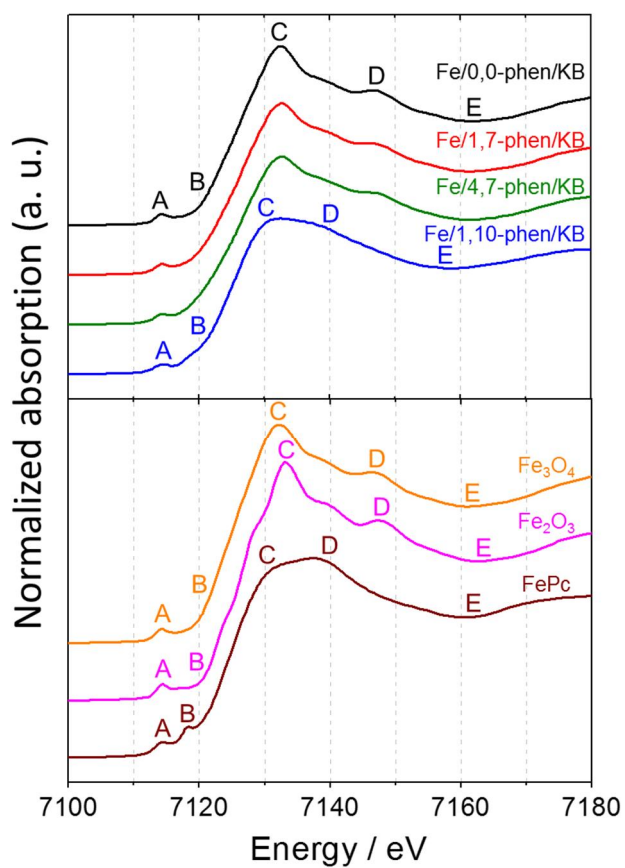
Figure 3.6. XANES spectra of Fe/pore filler/KB catalysts. (with the Fe_3O_4, Fe_2O_3 and FePc as reference)
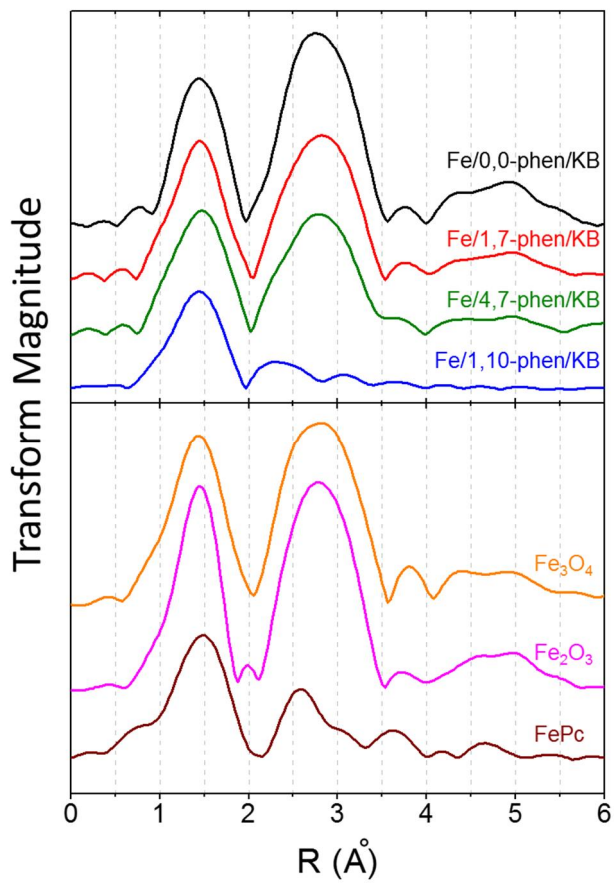
Figure 3.7. FT-EXAFS spectra of Fe/pore filler/KB catalysts. (with the Fe$_3$O$_4$, Fe$_2$O$_3$ and FePc as reference)
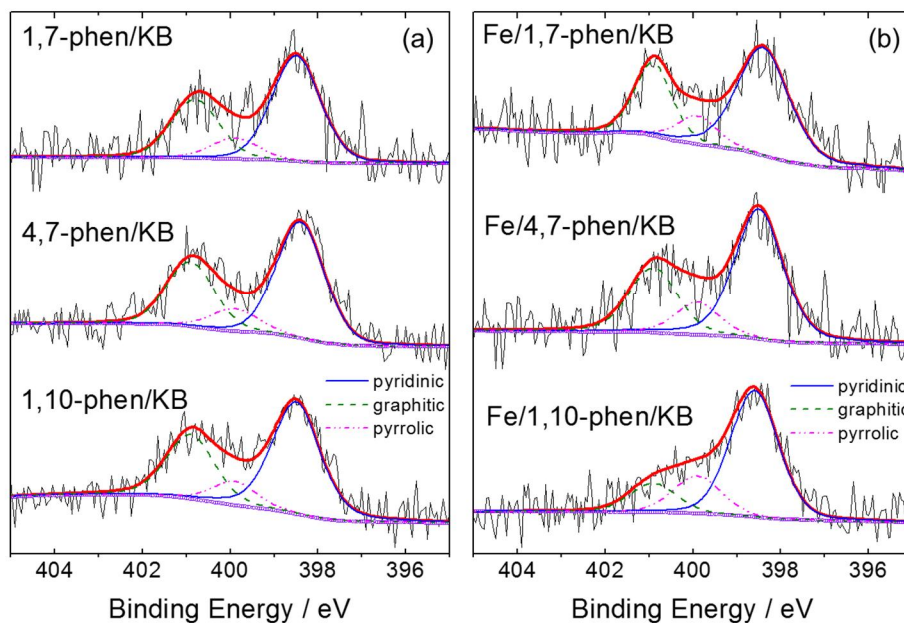
Figure 3.8. XPS N1s peaks and fitting results for the pyrolyzed catalysts:
(a) pore filler/KB catalysts and (b) Fe/pore filler/KB catalysts.

3.1.3 Electrochemical Measurements

The ORR activities of Fe/pore filler/KB samples were investigated using rotating disk electrode (RDE) measurements. The RDE polarization curves of catalysts in 0.1 M KOH clearly demonstrate that ORR activities depend on the impregnated precursor compounds during their synthetic process (**Fig. 3.9a**). Their onset potentials (E_{onset} is defined as the potential at 0.1 mA cm^{-2} of current density in this study) and half-wave potentials ($E_{1/2}$) are summarized in **Table 3** as activity parameters. At first, The N-containing-precursor catalyst groups (Fe/1,7-phen/KB, Fe/4,7-phen/KB and Fe/1,10-phen/KB) showed much improved ORR activities compared to Fe/0,0-phen/KB, N-free-precursor catalyst. Among those N-containing-precursor catalysts, however, their ORR activities varied again depending on the presence of Fe-N coordination in their precursor compounds. Two catalysts without Fe-N coordination (Fe/1,7-phen/KB and Fe/4,7-phen/KB) showed almost same ORR polarization curves with similar E_{onset} (0.89 and 0.90 V, respectively) and $E_{1/2}$ (0.74 and 0.74 V, respectively). With utilization of precursor with Fe-N coordination, Fe/1,10-phen/KB demonstrated superior ORR activity with higher E_{onset} (1.00 V) and $E_{1/2}$(0.87 V). Considering their similar Fe and N contents, their ORR activity deviation was originated from their Fe and N configuration, which is related to their active site. Therefore, we further investigated the relationship between the structure of the N dopant and ORR kinetics in those catalyst samples. Interestingly, there was a strong correlation between the ratio

of pyridinic N content to graphtic N content (P/G ratio) and the mass-transfer-corrected kinetic current density (j_K) at 0.85 V (**Fig. 3.10**). The P/G ratio and j_K value of Fe/1,10-phen/KB (4.38 and 9.56 mA cm^{-2}, respectively) were much bigger than those of Fe/1,7-phen/KB (2.08 and 0.36 mA cm^{-2}, respectively) and Fe/4,7-phen/KB (2.02 and 0.38 mA cm^{-2}, respectively). Considering that the Fe-free catalysts showed similar configurations of N dopant and ORR activities (**Fig. 3.9b** and **Table 3**), the existence of Fe-N coordination in their precursors acted as a crucial factor for ORR activity with affecting the Fe-N$_4$ active site formation during pyrolysis. The electron transfer numbers per O$_2$ calculated from the slopes of K-L plots [101] at 0.6 V (**Fig. 3.11**) also suggested that the Fe/1,10-phen/KB (3.98) had better reaction selectivity for the four-electron pathway compared to Fe/1,7-phen/KB (3.84) and Fe/4,7-phen/KB (3.84). This ORR performance trends was also maintained in the acidic condition (**Fig. 3.12**).

The best performing catalyst, Fe/1,10-phen/KB, exhibited a comparable ORR activity to commercial Pt/C electrocatalyst in alkaline condition (**Fig. 3.13a**), with a small half-wave potential difference (approx. 18 mV). Also in the acid electrolyte, Fe/1,10-phen/KB showed a considerable activity with an onset potential of 0.82 V. (**Fig. 3.13b**). A long-term durability tests of Fe/1,10-phen/KB and Pt/C catalyst were also conducted, involving potential cycling between 0.6 and 1.0 V up to 10,000 times in Ar-saturated 0.1 M KOH solution. Fe/1,10-phen/KB exhibited remarkably high stability with a nearly identical polarization curve even after 10,000 cycles, whereas a

significant activity loss was observed for Pt/C catalyst (**Fig. 3.14**). I also evaluated the feasibility of Fe/1,10-phen/KB catalyst for practical fuel cell applications with AEMFC single cell analysis with MEA test. **Fig. 3.15** shows the single cell performances of the MEA using Fe/1,10-phen/KB as a cathode catalyst. The maximum power density of Fe/1,10-phen/KB-based MEA was 197 mW cm^{-2}, which was about 84 % of peak power density for reference MEA with Pt/C cathode. This excellent single cell performances indicate that the Fe/1,10-phen/KB catalyst is a promising non-precious metal catalysts for AEMFC applications
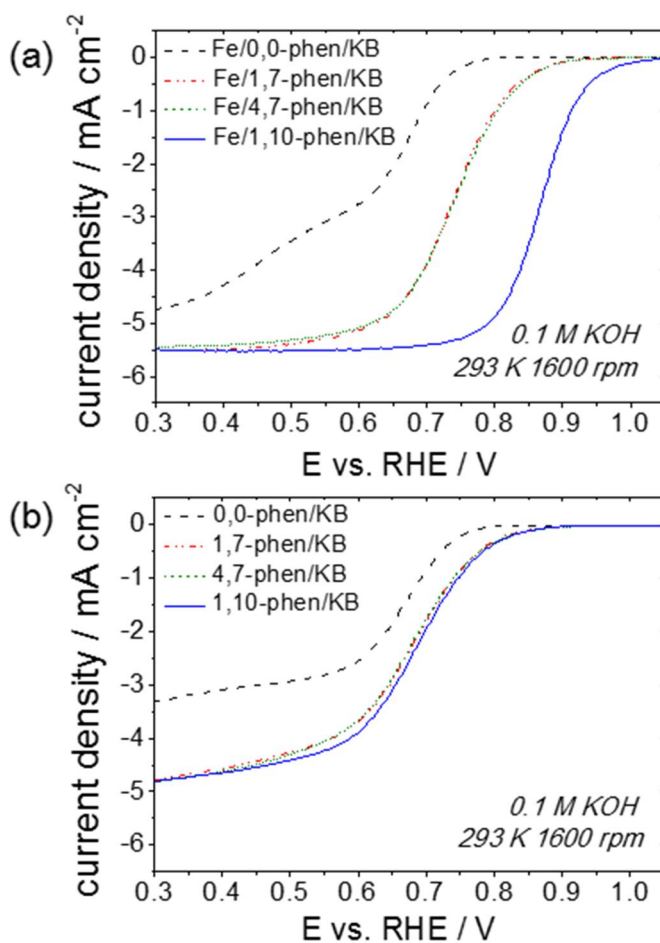
Figure 3.9. ORR measurements for the pyrolyzed catalysts in alkaline conditions: RDE polarization curves of (a) Fe/pore filler/KB and (b) pore filler/KB catalysts in O_2-saturated 0.1 M KOH with a scan rate of 5 mV sec^{-1}, 1600 rpm. Catalyst loading: 0.4 mg cm^{-2}

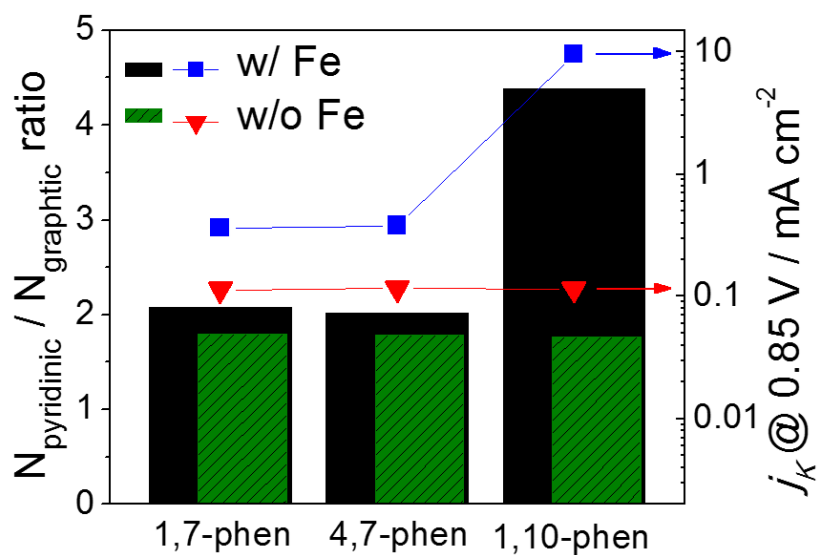**Figure 3.10. Correlation between the ratio of pyridinic N content to graphtic N content and the mass-transfer-corrected kinetic current density at 0.85 V versus the RHE.**
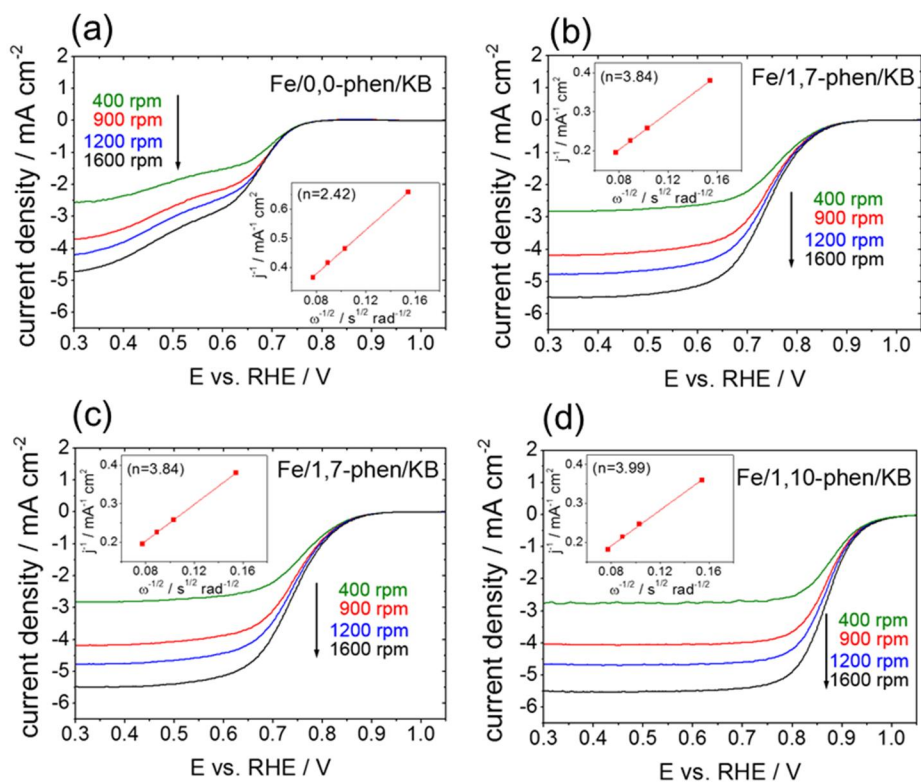
Figure 3.11. Koutecky-Levich analysis for Fe/pore filler/KB catalysts: RDE polarization curves for (a) Fe/0,0-phen/KB (b) Fe/1,7-phen/KB (c) Fe/4,7-phen/KB and (d) Fe/1,10-phen/KB in O_2-saturated 0.1 M KOH at a scan rate of 5 mV sec^{-1} with various electrode rotating rates (inset) Koutecky-Levich plot of J^{-1} vs $\omega^{-1/2}$ at 0.60 V vs RHE.
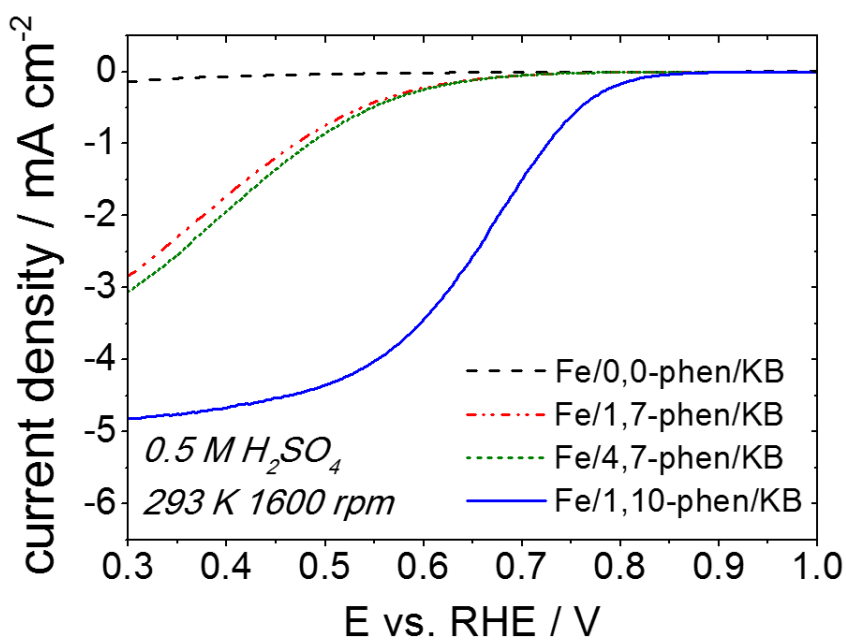
Figure 3.12. ORR measurements for the Fe/pore filler/KB catalysts in acid conditions: RDE polarization curves of Fe/pore filler/KB catalysts in O_2-saturated 0.5 M H_2SO_4 with a scan rate of 5 mV sec^{-1}, 1600 rpm. Catalyst loading: 0.4 mg cm^{-2}.
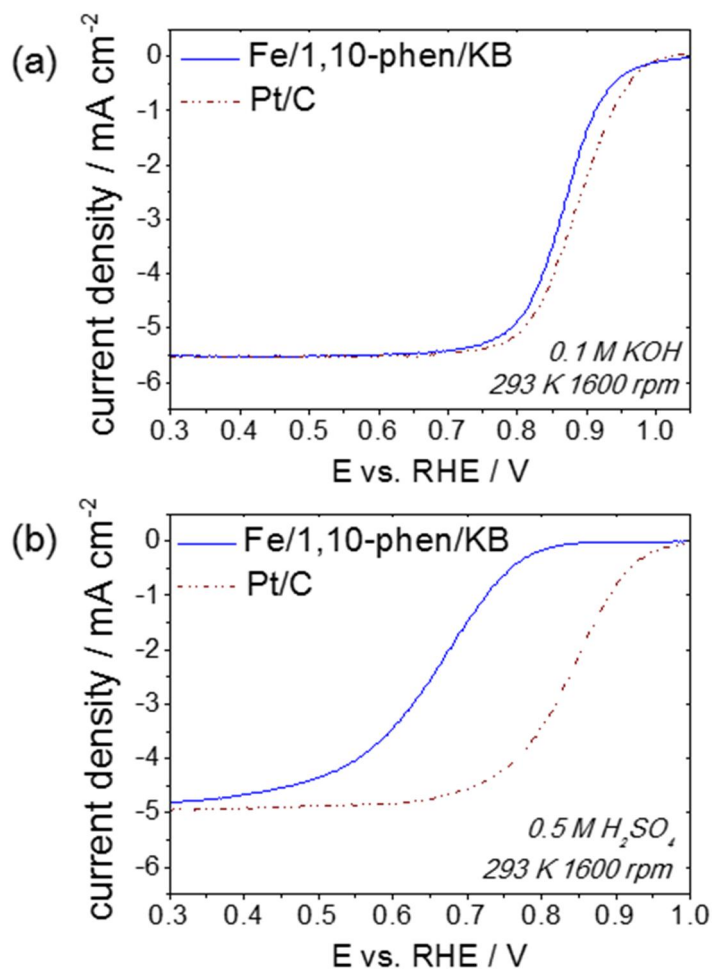
Figure 3.13. Comparative ORR activities Fe/1,10-phen/KB and Pt/C catalysts in half-cell conditions: RDE polarization curves of Fe/1,10-phen/KB with commercial Pt/C 20wt% catalyst in O_2-saturated (a) 0.1 M KOH and (b) 0.5 M H_2SO_4. The electrode rotation speed was 1600 rpm. Fe/pore filler/KB catalysts loading: 0.4 mg cm^{-2} and Pt/C loading: 0.02 mg$_{Pt}$ cm^{-2}.
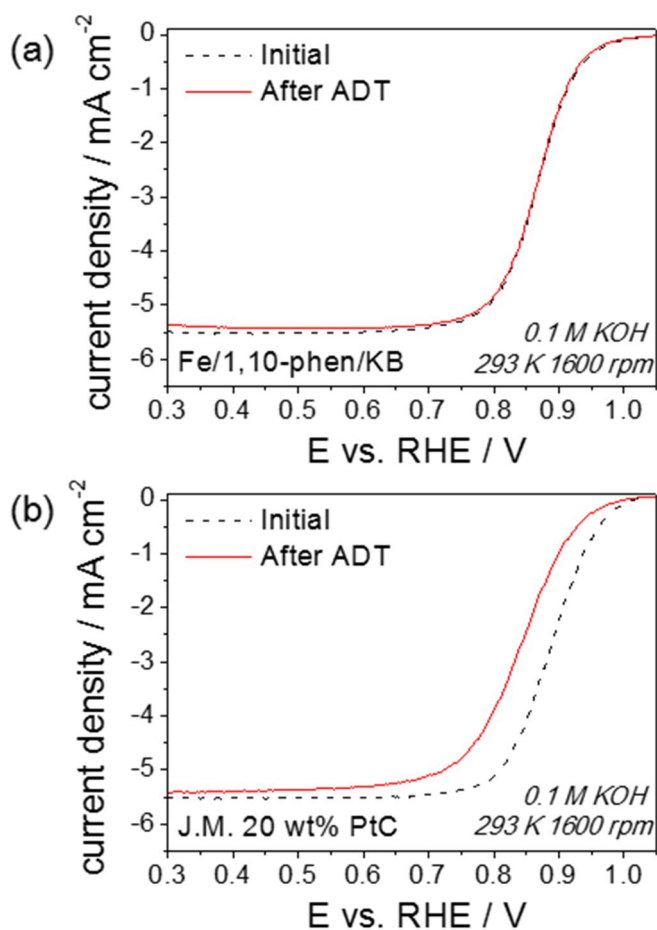
Figure 3.14. Long-term stability of Fe/1,10-phen/KB and commercial Pt/C catalysts: RDE polarization curves before/after accelerated durability test (ADT) for (a) Fe/1,10-phen/KB and (b) commercial Pt/C 20wt% catalyst. The electrode rotation speed was 1600 rpm in O_2-saturated 0.1 M KOH.
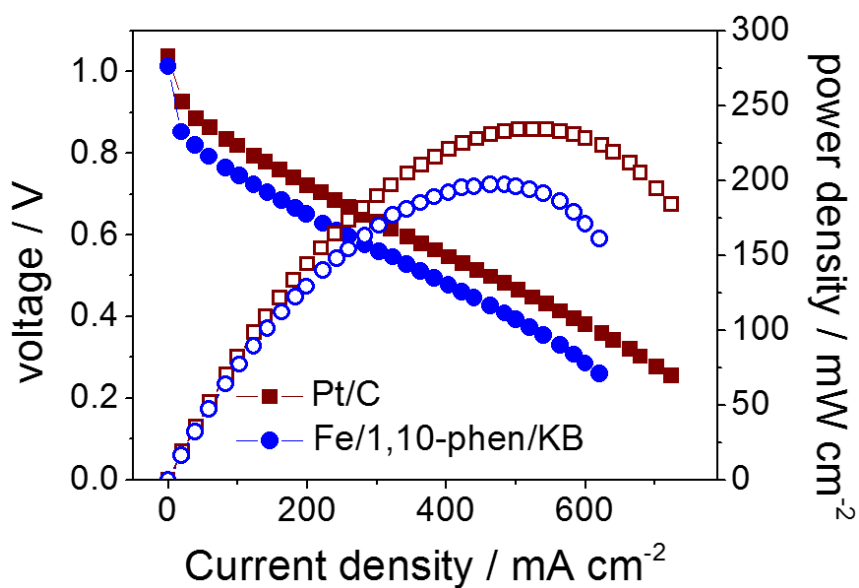
Figure 3.15. Comparative ORR activities Fe/1,10-phen/KB and Pt/C catalysts in single-cell conditions: Alkaline AEMFC single cell performances of MEAs with Fe/1,10-phen/KB and Pt/C cathode catalysts.

3.1.4 Precursor Coordination Effect on Active Site Formation

In the process of Fe-N-C catalyst synthesis, the main active sites are generally formed during high temperature pyrolysis. Therefore, the actual thermal behavior of Fe and N precursors during heat treatment is crucial for catalytic site formation. In this context, the weight change data of precursor compounds provides clues to the active site forming process with those precursors. Without Fe-N coordination (Fe/1,7-phen and Fe/4,7-phen), the complete gasification of phen precursors was observed below 300 °C, and the pyrolysis behaviors of these precursors were same as those of pure 1,7-phen and 4,7-phen (**Fig. 3.2**). With Fe-N coordination (Fe/1,10-phen), however, a significant portion of weight remained at high temperature condition unlike pure 1,10-phen. Due to above thermal behavior characteristics, their Fe and N configurations after pyrolysis were totally different, affecting the Fe-N_4 active site formation. First, Fe-N coordination helped the Fe atoms to be evenly distributed in the catalysts, with increasing the possibility of Fe-N_4 active site formation significantly (**Fig. 3.4** and **Fig. 3.5**). In the absence of Fe-N coordination, Fe was easily aggregated into particles without any physical disturbance from phen precursors after their gasification. However, when the Fe-N coordination existed in precursor, the Fe particle aggregation was suppressed due to physical interference of surrounding non-gasified phen precursor residues. In addition, the Fe-N coordination bonds in precursor improved the possibility of the Fe-N_4 site formation by locating N atom near Fe during heat

treatment (**Fig. 3.8**). Without coordination, N atoms were doped into carbon through the gasification of phen precursors during pyrolysis, and there was no Fe effect in determining N doping sites. Therefore, N configurations of Fe/1,7-phen/KB and Fe/4,7-phen/KB were almost same as those of 1,7-phen/KB and 4,7-phen/KB. In the case of using Fe-N coordination complex precursor (Fe/1,10-phen/KB), on the other hand, there existed a Fe effect on the doping position of N atoms, with maintaining the Fe-N distance of coordination complex (Fe/1,10-phen) during pyrolysis. Therefore, the relative amount of graphitic N of Fe/1,10-phen/KB, which is generally located in the middle of graphitic carbon and difficult to be adjacent to Fe, was significantly decreased compared to that of 1,10-phen/KB. As a result, Fe-N coordination helped N to be located in the pyridinic N position, which is more favorable for the active site formation than other N sites [95, 102].

3.2 Carbon Support Study

3.2.1 Carbon Support: Pore Structure

Monodisperse and size-tunable resorcinol–formaldehyde polymer (RFP) spheres were prepared using a sol-gel method from resorcinol and formaldehyde precursors in aqueous solution with ammonia catalyst (see experimental section for more details). After determining the spherical and monodisperse shapes of the as-synthesized RFPs using SEM (**Fig. 3.16a**), the RFP spheres were carbonized to resorcinol–formaldehyde carbon (RFC) with heat treatment under a N_2 atmosphere. The SEM image of these RFC spheres showed that the monodispersity was retained and that the size had shrunk after carbonization. This size shrinkage (from 301±10 nm to 206±10 nm) was probably due to radial contraction of RFP during the carbonization process (**Fig. 3.16a, b**). [103, 104]

Attempting to modulate the microporosity of the RFC spheres, a hot CO_2 treatment $(C\ (s) + CO_2\ (g) \rightarrow 2CO\ (g))$ was employed, in which the microporosity of the carbonaceous materials could be readily controlled by the activation time. The activated RFC spheres are denoted as RFC_CX, where X is the CO_2 activation time (e.g., 30, 120, and 240 min). During hot CO_2 treatment, the RFC_CX samples

decreased in size, from 206±10 before treatment to 196±14, 179±19, and 163±23 nm with CO_2 activation times of 30, 120, and 240 min, respectively (**Fig. 3.16b-e**). This size decreasing tendency in the RFC_CX samples was probably caused by the loss of carbon mass during CO_2 activation. The gradual development of porosity during prolonged hot CO_2 treatment was also confirmed by TEM images, in which the features of the RFC_C30, C120, and C240 samples were observed to be much less dense compared with the pristine RFC sphere (**Fig. 3.17**). The development of porosity in RFC_CXs was further determined by nitrogen sorption isotherm measurements (**Fig. 3.18** and **Table 4**). The increased vertical rise at low $P P_0^{-1}$ of type I isotherms with increasing hot CO_2 treatment time implied that the microporosity mainly developed in RFC during the CO_2 activation process. In addition, the enhanced micropore surface areas with CO_2 activation were actually determined by the non-local density functional theory (NLDFT) (462, 903, 1536, and 2374 $m^2 g^{-1}$ for RFC, RFC_C30, C120, and C240, respectively). It was noted that prolonged activation treatment led to the generation of mesopores, indicated as a type IV isotherm, especially in RFC_C240. Specific surface areas (SSAs), obtained using the Brunauer–Emmett–Teller (BET) method with N_2 as adsorbate, of 572, 938, 1766, and 2975 $m^2 g^{-1}$ were measured for RFC, RFC_C30, C120, and C240 samples, respectively, indicating that the CO_2 activation process effectively controlled the porosity of the RFC spheres (**Table 4**). In order to monitor the development of the pore structure

during CO_2 activation, the pore size distribution (PSD) in the activated RFC samples was determined with the NLDFT assuming a slit-pore geometry. According to the PSD curves in **Fig. 3.18b**, two peaks, at around 0.7 nm and 1.5 nm, appeared for all the activated RFC samples, with a third peak at around 2.5 nm present only for the RFC_C240 sample. Therefore, a series of RFC spheres with controlled microporosity had been prepared to investigate the effect of the pre-defined microporosities of the carbon supports on the formation of catalytic sites in Fe-N-C catalysts, which ultimately determines the ORR activity.
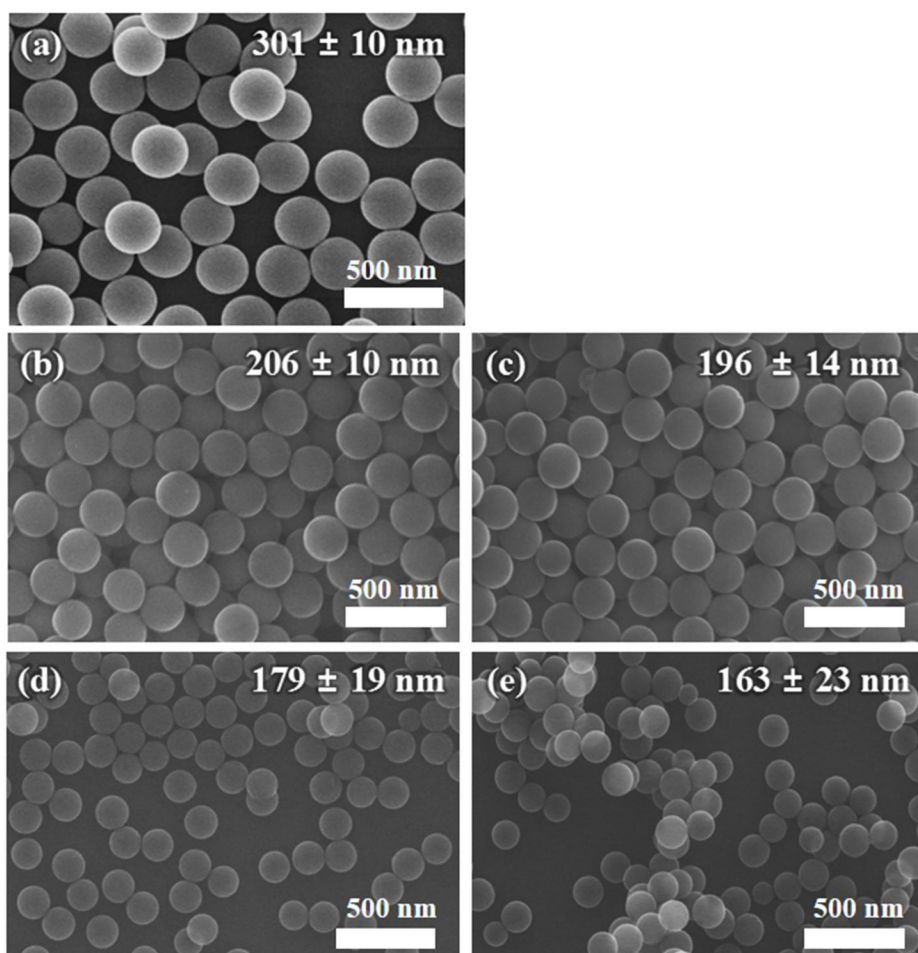
Figure 3.16. SEM images of prepared carbon supports: (a) RFP, (b) RFC, (c) RFC_C30, (d) RFC_C120, and (e) RFC_C240.
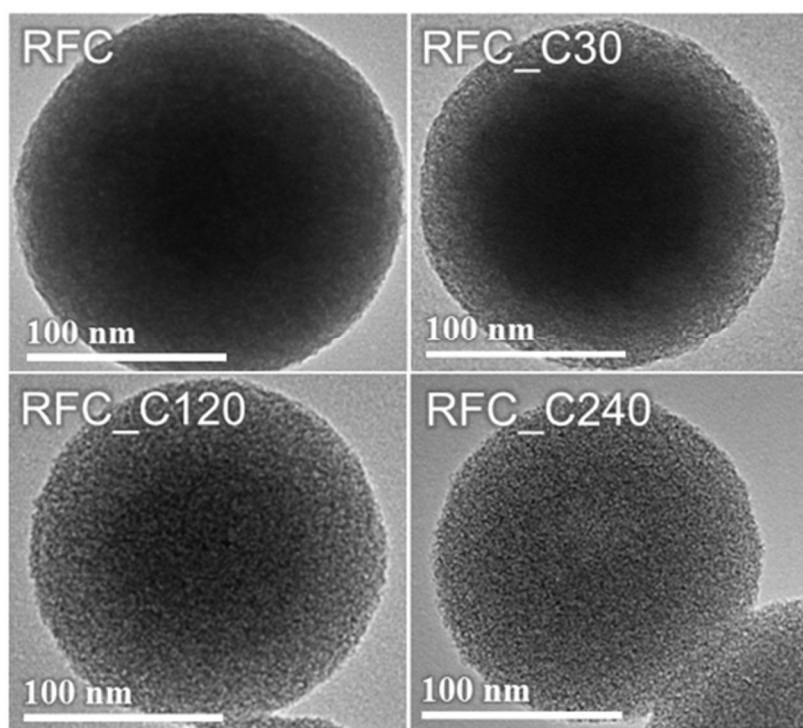
Figure 3.17. TEM images of prepared carbon supports.
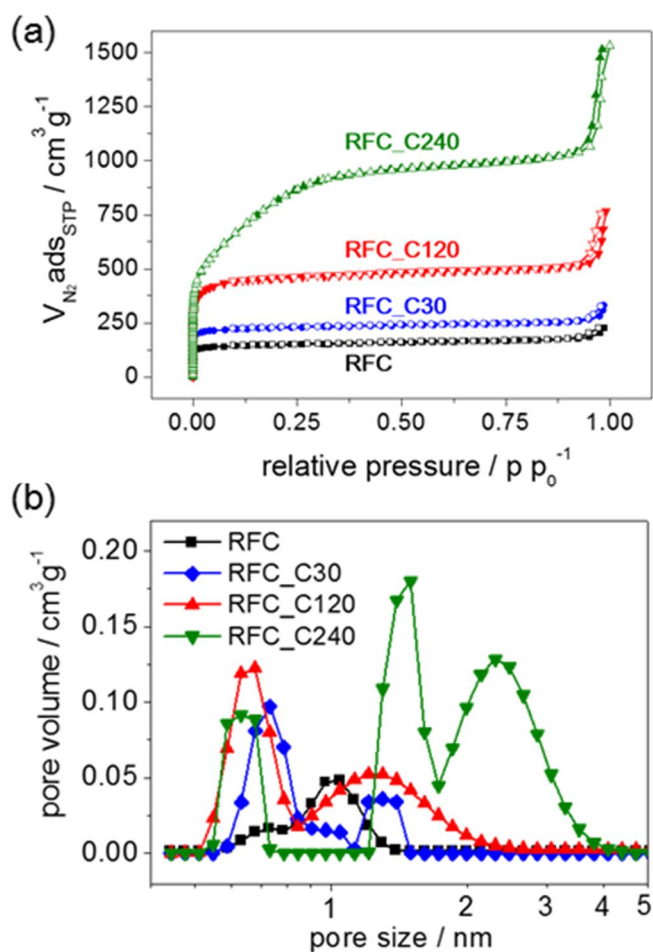
Figure 3.18. Pore structures of prepared carbon supports: (a) Nitrogen adsorption-desorption isotherms for RFC_CXs and (b) BET isotherm analyses on incremental pore volume as the function of pore size in RFC_CXs.

Table 4. Physical and chemical properties of RFC_CX and Fe-N-RFC_CX samples.

Sample	S_{BET} (m^{2}g^{-1})	$S_{micropore}$[a] (m^{2}g^{-1})	V_{Total}[b] (cm^3 g^{-1})	Fe-ICP (wt%)	N-EA (wt%)	Half-wave potential (V vs. RHE)
RFC	572	462	0.348	No detected	1.09	-
RFC_C30	938	903	0.555	No detected	1.08	-
RFC_C120	1766	1536	1.170	No detected	0.91	-
RFC_C240	2975	2374	2.230	No detected	0.80	-
Fe-N-RFC	172	142	0.231	0.49	1.29	0.75
Fe-N-RFC_C30	877	824	0.513	0.52	2.02	0.86
Fe-N-RFC_C120	1537	1490	0.895	0.53	2.35	0.89
Fe-N-RFC_C240	2913	2169	1.822	0.57	2.84	0.91

[a] The micropore surface area was obtained by the NLDFT method. [b] Total pore volume was determined at P/P$_0$=0.99.

3.2.2 Physical Characterizations of Fe-N-C Catalysts

In order to synthesize the Fe-N-RFC_CX samples, an iron precursor with a pore filler was impregnated into the microporosity- controlled RFC samples, and the mixed powder samples were subsequently pyrolyzed under an inert atmosphere. After heat treatment, only carbon-related peaks were shown in XRD patterns for as-prepared Fe-N-RFC_CX samples except Fe-N-RFC (**Fig. 3.19b**). Fe-N-RFC showed distinct Fe and Fe_3O_4 crystal peaks, as well as a well-developed graphitic-carbon-phase peak at approx. 26°, probably originating from Fe-particle-induced graphitization during heat treatment [105]. Considering that negligible crystalline Fe-related phases appeared in the other as-prepared samples, less porous features in the RFC samples would probably result in more aggregated Fe nanoparticles on the carbon surface. As my main concern was the $Fe-N_4$ ORR active sites formed within the micropores, Fe and Fe_3O_4 particles from excess Fe precursor, which might block the active sites, were removed by acid post-treatment, and the leached powders were heat treated again under inert conditions. The XRD patterns of the final Fe-N-RFC_CX series showed that the Fe and Fe_3O_4 crystals were successfully removed from all samples (**Fig. 3.19c**). The morphological features of the Fe-N-RFC_CX samples were characterized by SEM and TEM analyses. According to the SEM images (**Fig. 3.20**), the spherical shape, smooth surface, and uniform sizes of the RFC_CX samples had been maintained during the Fe-N-RFC_CX synthetic processes. In addition, the density of the features in the Fe-

N-RFC_CX samples were similar to their corresponding RFC_CX samples, as shown by the TEM images, while more porous features were clearly observed for the more activated samples, as in the RFC_CX samples (**Fig. 3.17** and **Fig. 3.21**). The elemental distributions were further examined using an EFTEM equipped with an electron energy-loss spectroscope (EELS). According to the elemental mapping of C, Fe and N on the Fe-N-RFC_C240 (**Fig. 3.22**), the Fe and N were homogeneously distributed in the resultant catalysts.

The porosity features of Fe-N-RFC_CX samples were further characterized by nitrogen sorption measurements. The nitrogen sorption isotherms of Fe-N-RFC_CXs showed similar features to those of RFC_CXs (**Fig. 3.18a** and **Fig. 3.23a**). SSAs of 172, 877, 1537, and 2913 $m^2\,g^{-1}$ were measured for Fe-N-RFC, RFC_C30, C120, and C240 samples, respectively. The micropore surface areas determined by the t-method for the Fe-N-RFC, Fe_N_RFC_30, C120, and C240 samples were 142, 824, 1490, and 2169 $m^2\,g^{-1}$, respectively. Even after impregnation and multiple heating processes, more than 90% of the microporosity of the Fe-N-RFC_CX samples was maintained, except for in the Fe-N-RFC sample (**Table 4**). According to PSD analysis (**Fig. 3.23b**), while a substantial portion of the micropores remained after the syntheses of samples Fe-N-RFC_C30, C120, and C240, they had completely disappeared in Fe-N-RFC. These pore structure changes after the pyrolysis might be attributed to residual materials from the impregnated pore filler. The additional mesoporosity of Fe-N-

RFC_C240, which had come from the prolonged activation process of carbon supports, was remained intact after Fe and N doping processes, implying the carbon pore structures within mesopore region was unaffected by the heat treatments.

To compare the Fe and N doping densities in each sample, the quantitative analysis for the Fe and N was conducted. The Fe doping contents measured by ICP-AES were 0.49, 0.52, 0.53, and 0.57 wt% for Fe-N-RFC, Fe-N-RFC_C30, C120, and C240, respectively (**Fig. 3.24** and **Table 4**). This showed the gradual increase in Fe content with increasing sample activation time. Furthermore, nitrogen incorporation was verified by elemental analysis. Before discussing the nitrogen contents for Fe-N-RFC_CX samples, the nitrogen contents of the parent RFC_CX samples should be addressed first. As shown in **Fig. 3.24**, RFC possessed some nitrogen (1.09 wt%) in the matrix, which could originated from ammonia catalyst during its synthesis [103]. According to elemental analysis data, the nitrogen contents in RFC_C30, C120, and C240 were lower than RFC (1.08, 0.91, and 0.80 wt%, respectively), probably resulting from the loss of nitrogen moieties from the carbon matrix during prolonged CO_2 activation. After the Fe and N doping process, the N contents of Fe-N-RFC, and Fe-N- RFC_C30, C120, and C240, were measured as 1.29, 2.02, 2.35, and 2.84 wt%, respectively (**Fig. 3.24** and **Table 4**). Considering the initial nitrogen amounts in the RFC_CX series, the increases in incorporated N content during the doping process were 0.20, 0.94, 1.44, and 2.04 wt% for Fe-N-RFC and Fe-N-RFC_C30, C120, and

C240, respectively. This result indicated that more nitrogen was incorporated into more activated carbon matrices.

To characterize the chemical state of nitrogen within the carbon matrix, XPS analysis was performed. High-resolution N1s XPS spectra of the Fe-N-RFC_CX samples (**Fig. 3.25a**) were deconvoluted into four nitrogen components (**Fig. 3.25b**): pyridinic N (approx. 398.5 eV), pyrrolic N (approx. 399.9 eV), graphitic N (approx. 401.2 eV), and oxidized N (approx. 402.5 eV). Interestingly, the relative amounts of pyridinic nitrogen increased with increasing activation of the carbon templates (27.7, 31.7, 33.6, and 36.2% for Fe-N-RFC and Fe-N-RFC_C30, C120, and C240, respectively), while those of graphitic N decreased (34.0, 32.0, 30.3, and 27.8%, respectively) (**Fig. 3.25c** and **Table 5**). Pyridinic nitrogen is located at the edge of the carbon matrix, and the edge sites in carbon supports are increased through the activation process. Therefore, the portion of pyridinic N after doping process in this study was likely to be controlled by activation of parent carbon supports. In contrast, the chemical state of the Fe species was not detected by XPS measurements, probably due to the low concentration of Fe (below 0.13 at% in the bulk sample), which was near the detection limit of XPS.
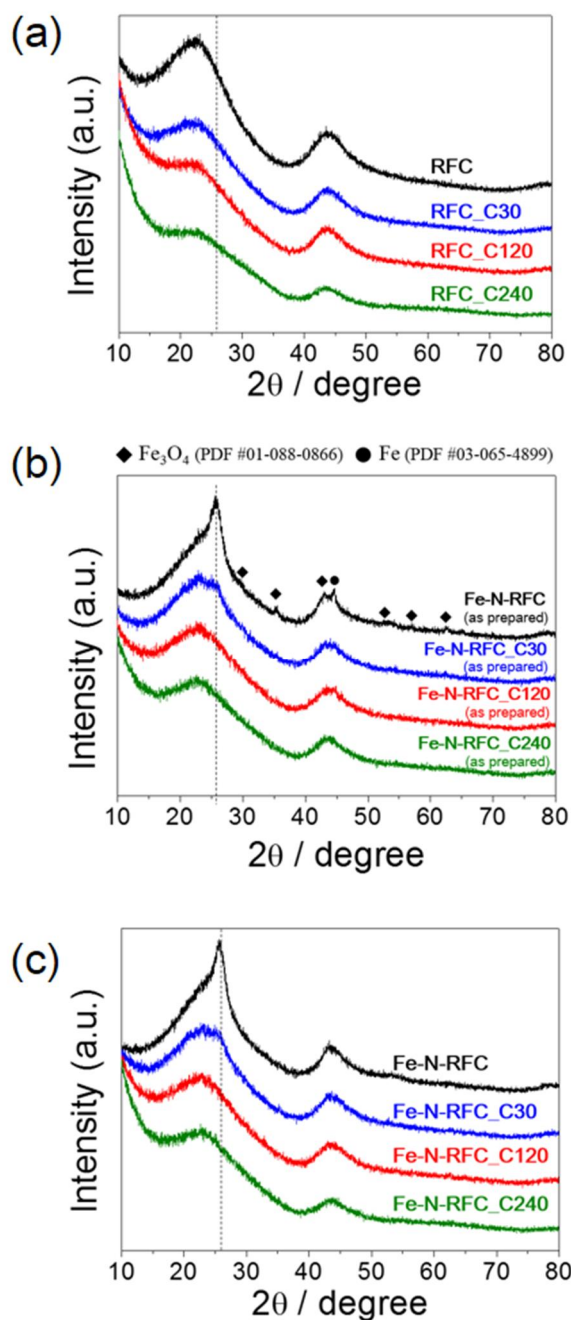
Figure 3.19. XRD patterns in each step of synthesis: (a) RFC_CXs, (b) as-prepared Fe-N-RFC_CXs; before acid leaching step, (c) Fe-N-RFC_CXs.
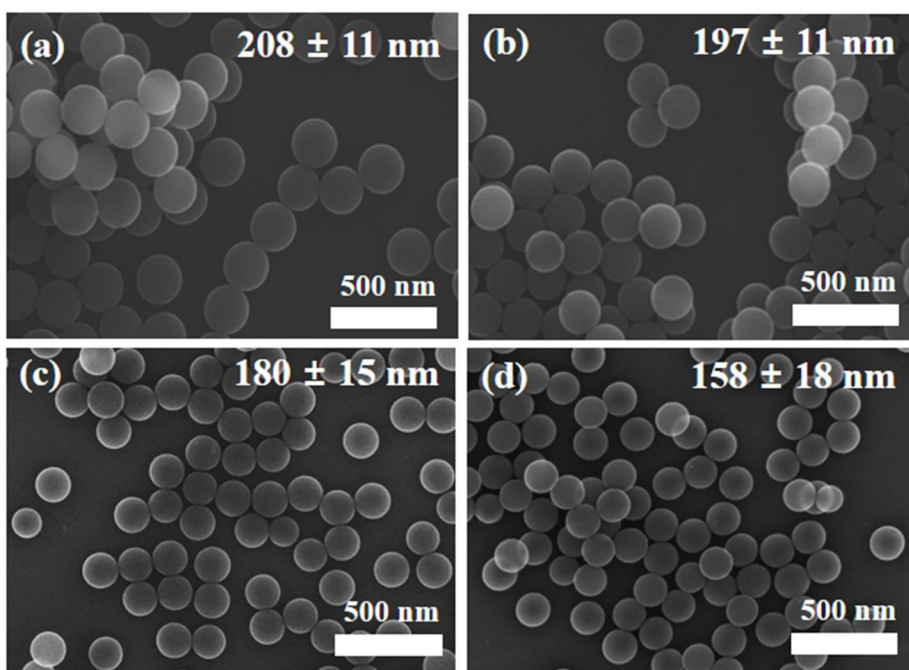
Figure 3.20. SEM images of synthesized catalysts: (a) Fe-N-RFC, (b) Fe-N-RFC_C30, (c) Fe-N-RFC_C120, and (d) Fe-N-RFC_C240.
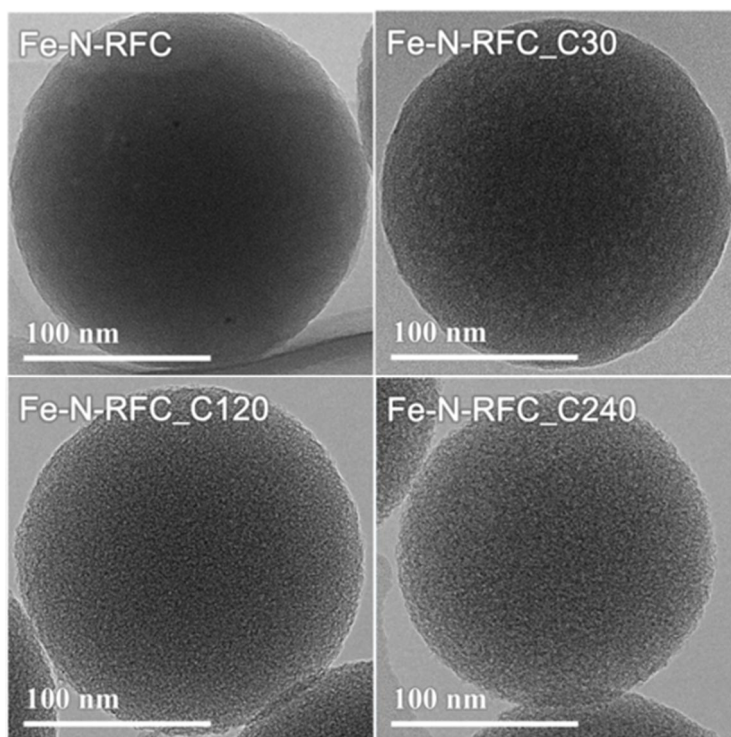
Figure 3.21. TEM images of synthesized catalysts.
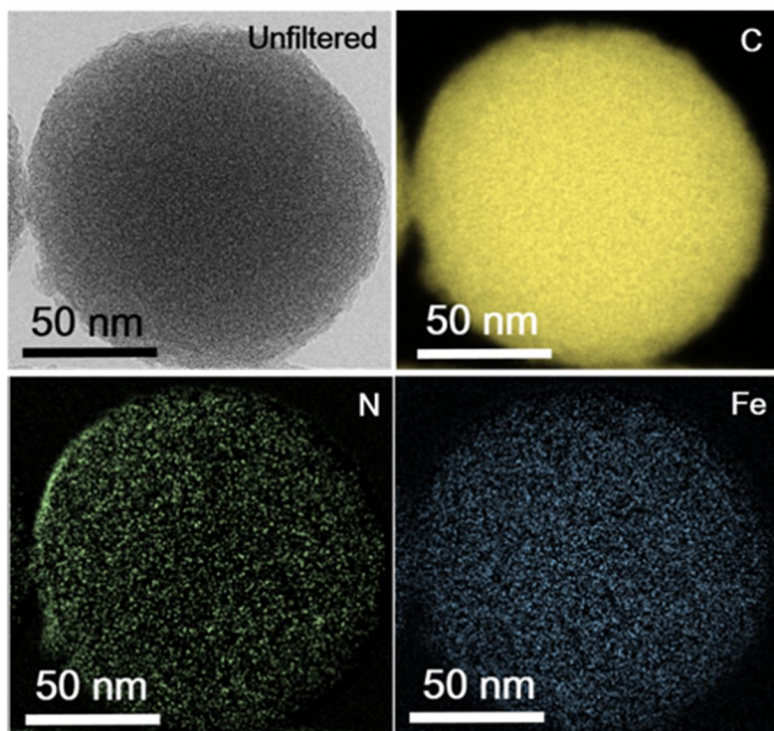
Figure 3.22. Energy-filtered TEM elemental mapping images for Fe-N-RFC_C240: Sequence of unfiltered image and C, N, Fe elemental maps.
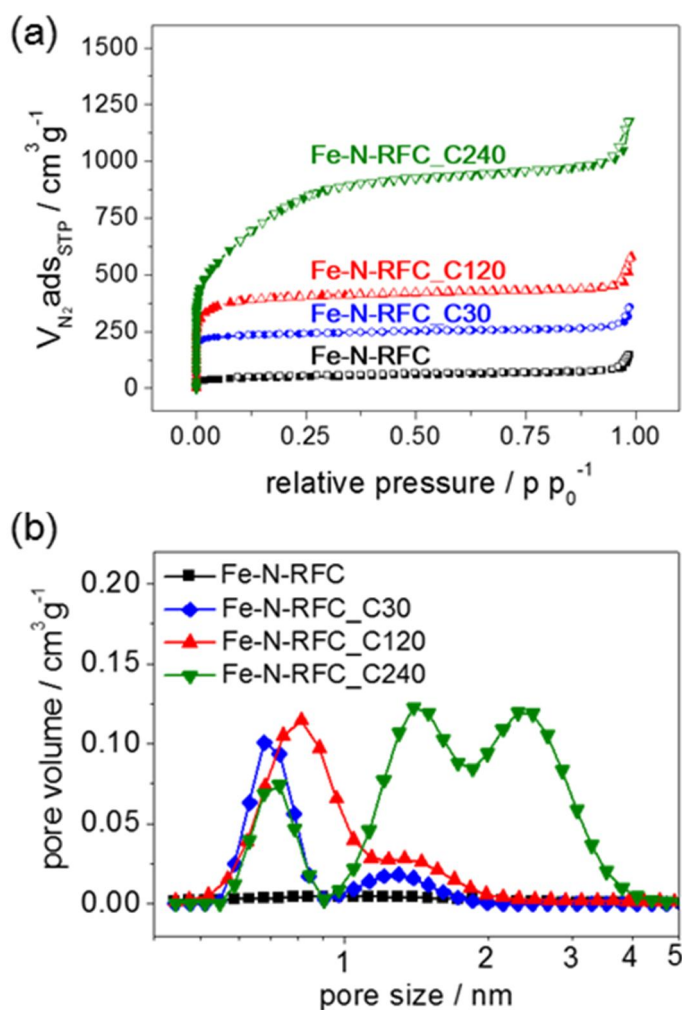
Figure 3.23. Pore structures of synthesized catalysts: (a) Nitrogen adsorption-desorption isotherms for Fe-N-RFC_CXs and (b) BET isotherm analyses on incremental pore volume as the function of pore size in Fe-N-RFC_CXs.
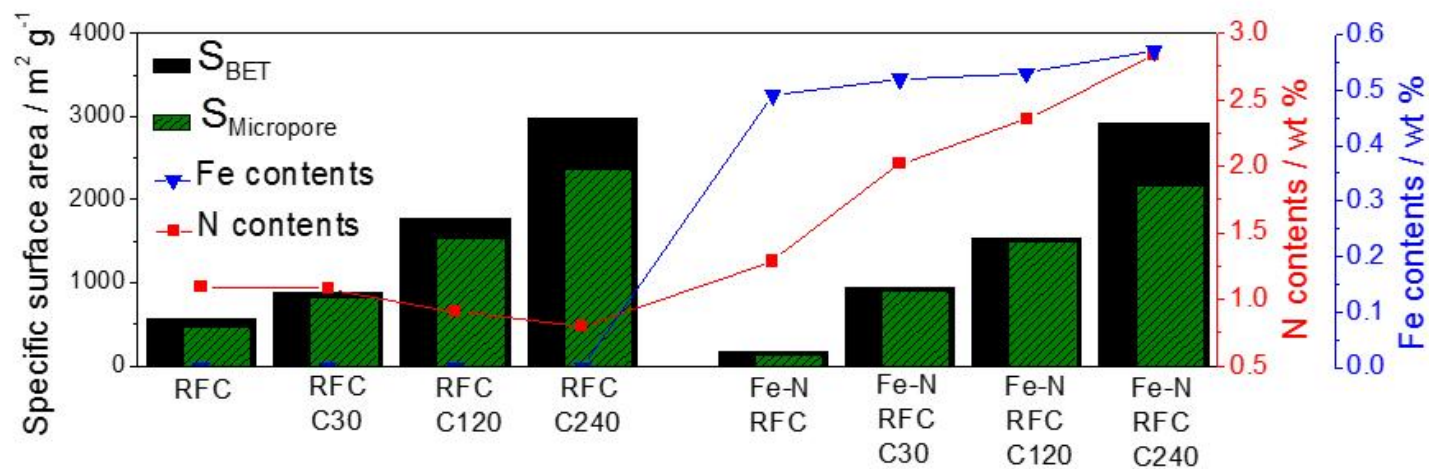
Figure 3.24. Correlation between the BET & micropore specific surface area and N & Fe contents of RFC_CXs and Fe-N-RFC-CXs.
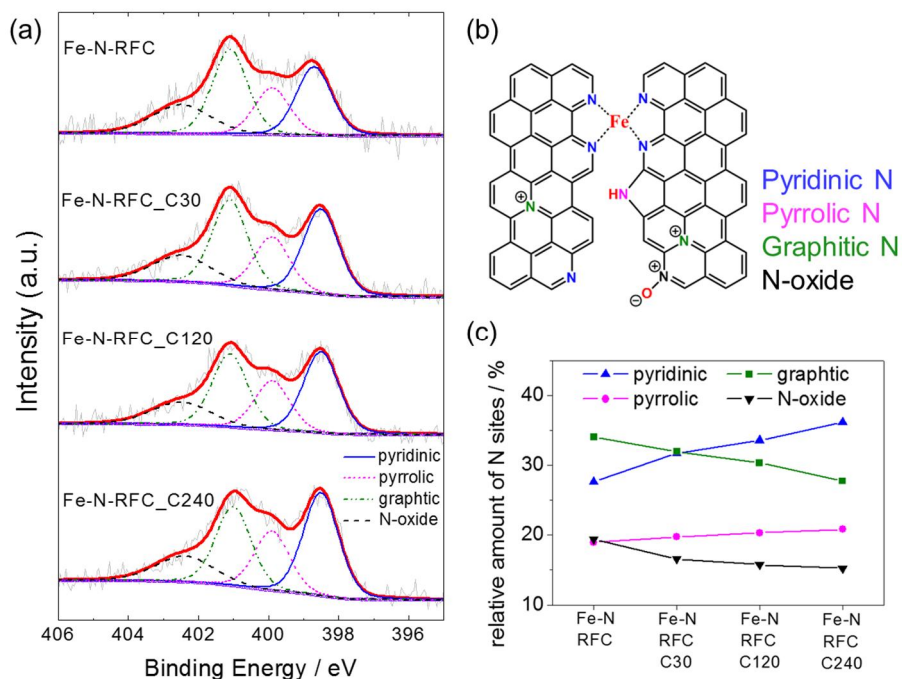
Figure 3.25. XPS N1s analysis for synthesized catalysts: (a) XPS N1s peaks and fitting results for Fe-N-RFC_CX samples, (b) their structural representation showing N-containing functionalities on carbon surface based on N1s electrons, and (c) corresponding relative amount of N sites for Fe-N-RFC_CXs.

Table 5. Relative N sites for Fe-N-RFC_CXs from the fitting results of XPS N1s peaks.

Sample	relative N site (%)			
	pyridinic	pyrrolic	graphitic	N-oxide
Fe-N-RFC	27.7	18.9	34.0	19.4
Fe-N-RFC_C30	31.7	19.7	32.0	16.6
Fe-N-RFC_C120	33.6	20.3	30.3	15.8
Fe-N-RFC_C240	36.2	20.8	27.8	15.2

3.2.3 Electrochemical Measurements

The ORR activities of the Fe-N-RFC_CXs were first investigated by CV in Ar-saturated and O_2-saturated 0.1 M KOH at a scan rate of 50 mV s^{-1} (**Fig. 3.26a**). The dotted-line voltammograms measured in Ar-saturated electrolyte showed a double-layer capacity current without any cathodic peak within the scan range. In contrast, well-defined cathodic peaks were found in all catalysts for CV measured in O_2-saturated electrolyte, suggesting pronounced ORR activity in these samples. The peak potentials moved in the positive direction, until saturation at 0.83 V, with increasing CO_2 activation of the carbon supports (0.71, 0.77, 0.83, and 0.83 V for Fe-N-RFC, and Fe-N-RFC_C30, C120, and C240, respectively). Further investigation of the ORR kinetics of the Fe-N-RFC_CXs samples was carried out using a RDE technique. The polarization curves obtained in O_2-saturated 0.1 M KOH (**Fig. 3.26b**) showed that the half-wave potentials also moved in a positive direction with increasing hot CO_2 treatment times of the carbon templates (0.75, 0.86, 0.89, and 0.91 V for Fe-N-RFC, and Fe-N-RFC_C30, C120, and C240, respectively), confirming that ORR activity was higher in the carbon supports with more developed pore structures. In order to verify the active site difference between samples, I also investigated the correlation between the N dopant and ORR kinetics in the Fe-N-RFC_CX series. As a kinetic parameter, kinetic current densities (j_K) at 0.85 V vs. RHE were derived from the mass-transport correction in the RDE data. The j_K values and the overall N contents in Fe-N-

RFC_CXs increased with longer activation times for the initial carbon templates (**Fig. 3.27**).

To further investigate the ORR kinetics of the Fe-N-RFC_CXs, the electron transfer numbers per O_2 were analysed on the basis of the K–L equations [101]. From the slopes of these plots at 0.60 V, the electron transfer numbers were calculated to be 3.68, 3.83, 3.92, and 3.99 for Fe-N-RFC, Fe-N-RFC_C30, C120, and C240, respectively (**Fig. 3.28**). This result indicated that the ORR proceeded along a more favorable four-electron pathway in catalysts derived from a carbon support with high microporosity. I also performed RDE measurements under acidic conditions (0.5 M H_2SO_4) to check whether the performance trends changed with pH. **Fig. 3.29a** shows that the overall trend in ORR performance of the catalyst samples was maintained in acidic electrolyte.

With the aim of verifying the Fe-N_4 active site structure in my catalysts, I further conducted RDE experiments in 0.1 M KOH containing 10 mM KCN. CN^- ions are known to strongly interact with Fe and, therefore, cause ORR inhibition on Fe-N_4 active sites [102, 106, 107]. As shown in **Fig. 3.29b**, introduction of CN^- ions shifted the ORR polarization curves toward negative potential and decreased the diffusion limited current. The impaired ORR activity in presence of CN^- ion indicates that the main active sites in my catalysts is Fe-N_4 structure, and this correlates with the tendency of Fe and N contents, amount of pyridinic N site, and ORR activity within Fe-N-RFC, Fe-N-RFC_C30, C120, and C240 samples (**Fig. 3.27**, **Table 4** and **Table 5**).

The best performing catalyst, Fe-N-RFC_C240, gave more improved ORR activity compared to Fe/1,10-phen/KB catalyst, with even ~18 mV higher half-wave potential than a commercial Pt/C electrocatalyst in 0.1 M KOH solution (**Fig. 3.30a**). Even in acidic media, Fe-N-RFC_C240 showed significant activity, with an onset potential of 0.84 V, although it was still lower than that of commercial Pt/C (**Fig. 3.30b**). I also performed chronoamperometry measurements in 0.1 M KOH solution with the injection of methanol to verify the methanol tolerance of my catalyst. While a significant methanol oxidation current was observed for Pt/C, no response was detected in the case of Fe-N-RFC_C240 (**Fig. 3.31a**). These results clearly showed that Fe-N-RFC_C240 was tolerant to methanol crossover and could be used as a cathode catalyst in a direct methanol fuel cell using an alkaline electrolyte. The long term stability of Fe-N-RFC_C240 was also confirmed by accelerated durability tests (ADTs) using the DOE protocol. Even after 10,000 cycles, negligible performance decay was observed in the Fe-N-RFC_C240 catalyst, suggesting outstanding stability (**Fig. 3.31b**).
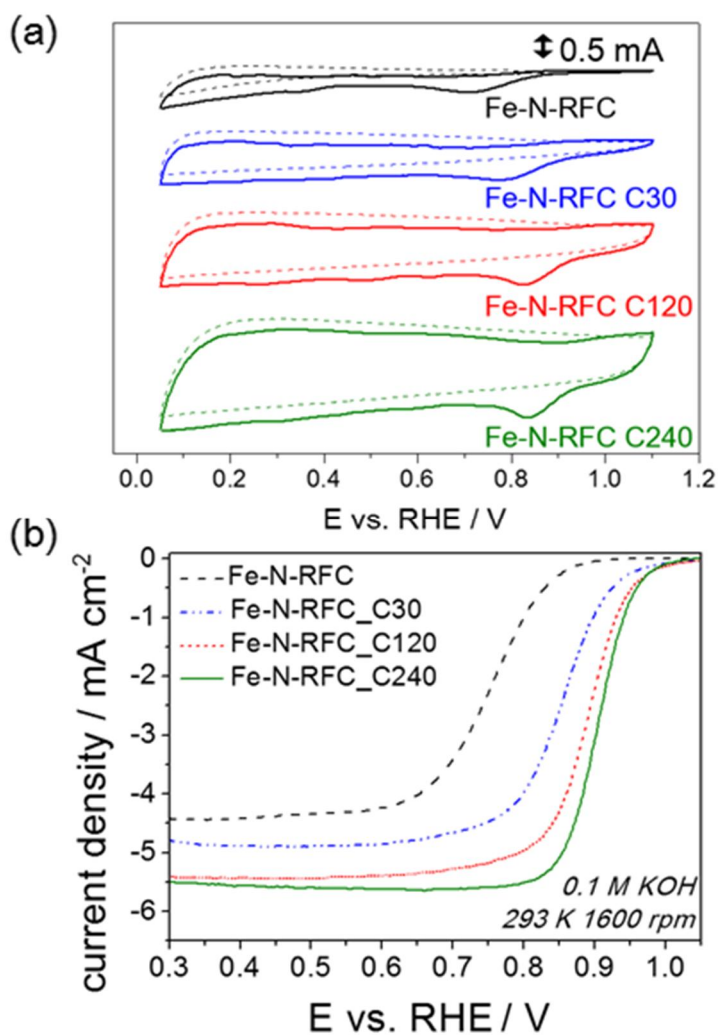
Figure 3.26. ORR measurements for the Fe-N-RFC_CXs in alkaline conditions: (a) Cyclic voltammograms of Fe-N-RFC_CXs in O_2 (solid lines) and N_2 (dash lines) saturated 0.1 M KOH solution. (b) RDE polarization curves of Fe-N-RFC_CXs at a rotating rate of 1600 rpm. Catalyst loading: 0.5 mg cm^{-2}
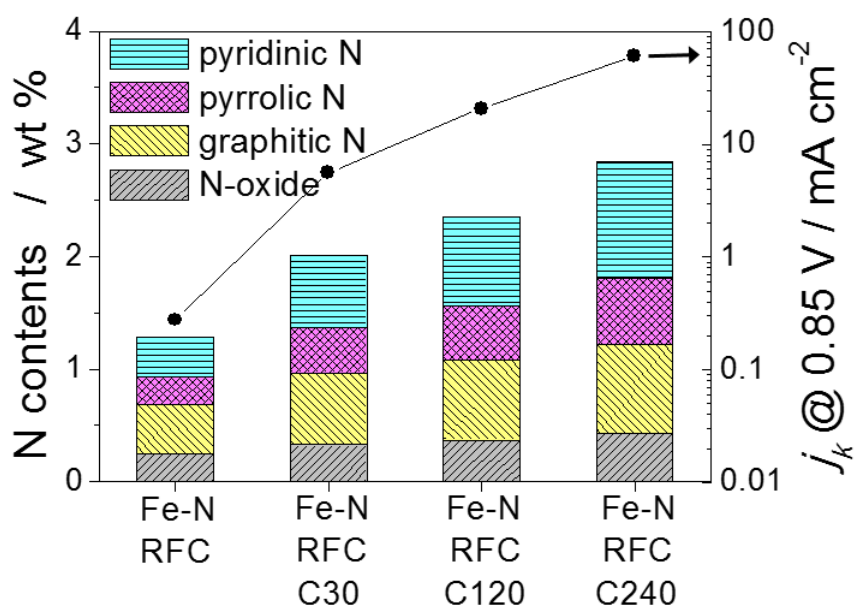
Figure 3.27. Correlation between the N contents of four configurations and the mass-transfer-corrected kinetic current density at 0.85 V versus RHE.
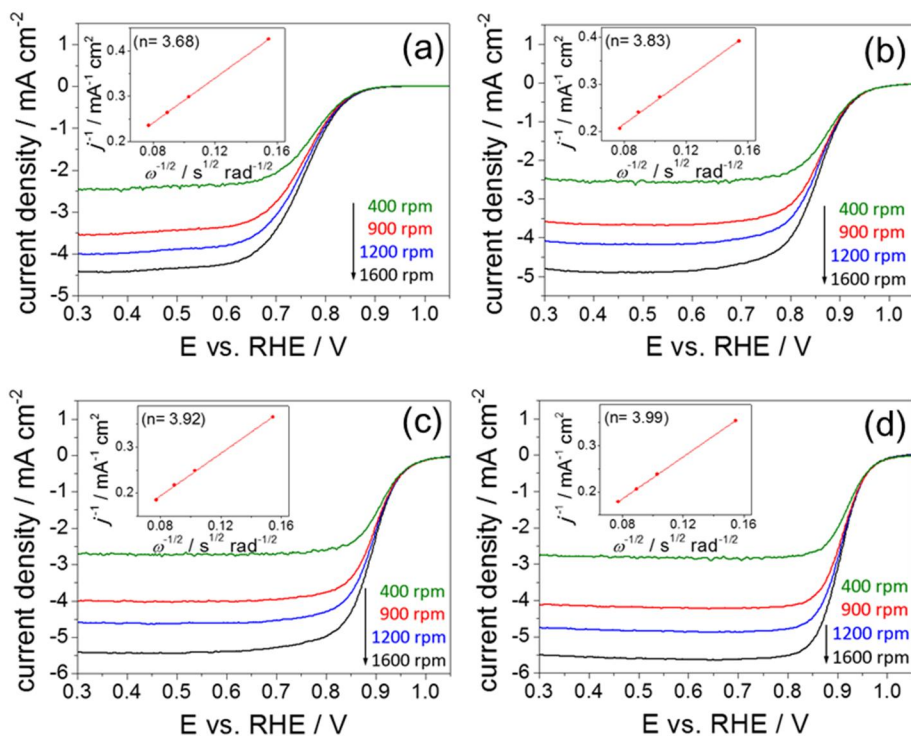
Figure 3.28. Koutecky-Levich analysis for Fe-N-RFC_CXs catalysts: RDE polarization curves for (a) Fe-N-RFC (b) Fe-N-RFC_C30 (c) Fe-N-RFC_C120 and (d) Fe-N-RFC_C240 in O_2-saturated 0.1 M KOH at a scan rate of 5 mV sec^{-1} with various electrode rotating rates (inset) Koutecky-Levich plot of J^{-1} vs $\omega^{-1/2}$ at 0.60 V vs RHE.
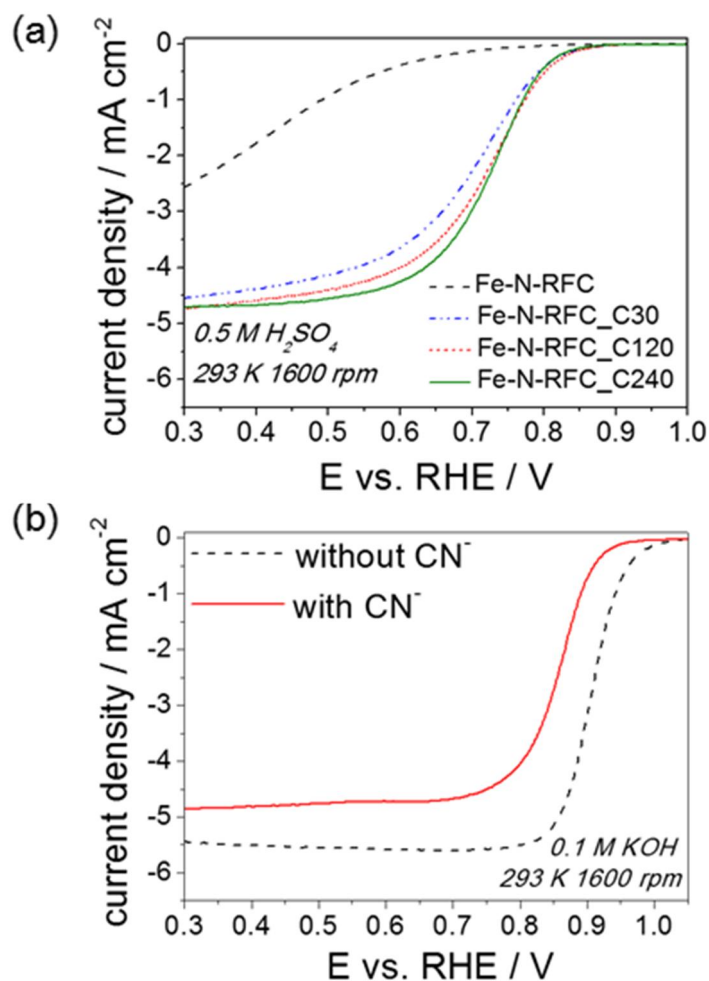
Figure 3.29. ORR measurements for the Fe-N-RFC_CXs in acid conditions and cyanide-ion poisoning test for Fe-N-RFC_C240: (a) RDE polarization curves of Fe-N-RFC_CX in O_2-saturated 0.5 M H_2SO_4 with a scan rate of 5 mV sec^{-1}, 1600 rpm. (b) RDE polarization curves of Fe-N-RFC_C240 with/without cyanide ions (10 mM KCN).
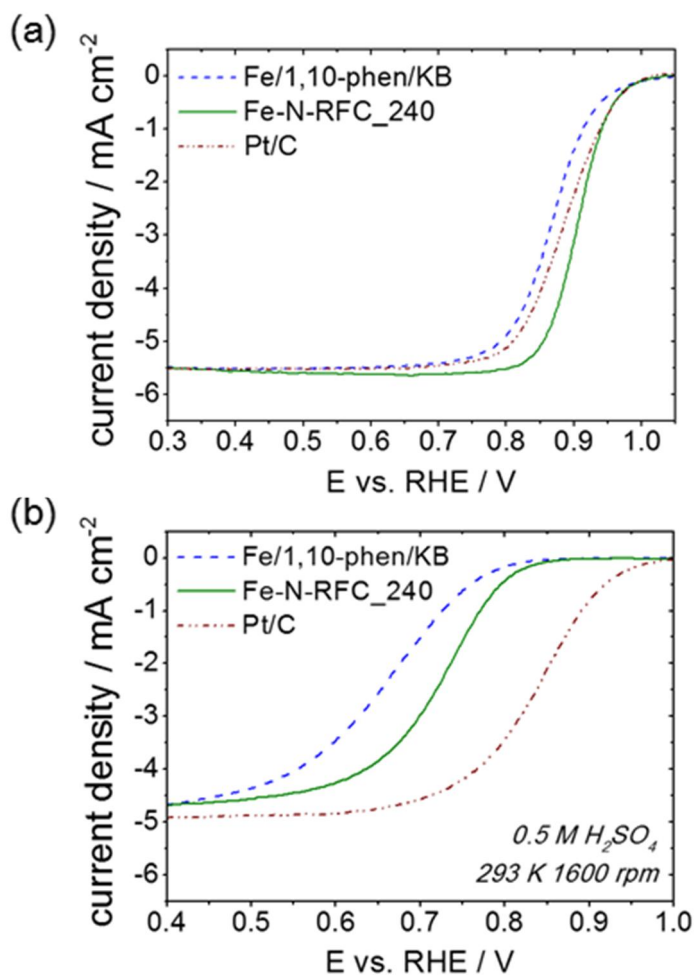
Figure 3.30. Comparative ORR activities Fe/1,10-phen/KB, Fe-N-RFC_C240 and Pt/C catalysts: RDE polarization curves of Fe-N-RFC_C240, Fe/1,10-phen/KB and commercial Pt/C 20wt% catalyst in O_2-saturated (a) 0.1 M KOH and (b) 0.5 M H_2SO_4. Fe-N-RFC_C240 catalyst loading: 0.5 mg cm^{-2} Fe/1,10-phen/KB catalyst loading : 0.4 mg cm^{-2} and Pt/C loading: 0.02 mg$_{Pt}$ cm^{-2}.
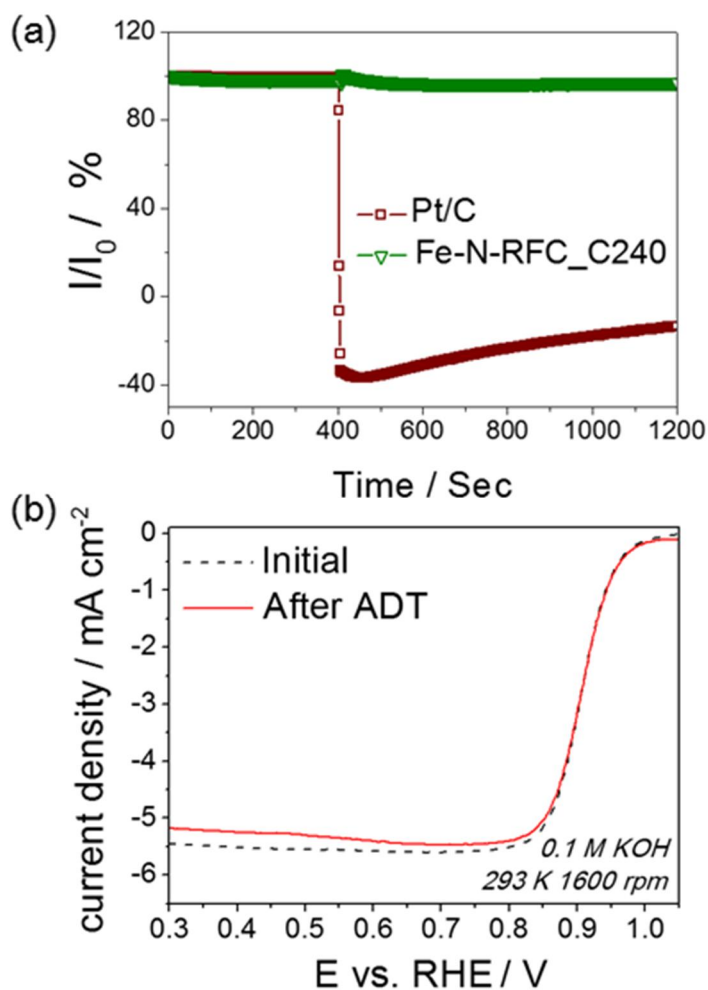
Figure 3.31. Methanol tolerance and long-term stability of Fe-N-RFC_C240: (a) Chronoamperometric responses at 0.7 V vs RHE with injection of methanol at 400 sec (b) RDE polarization curves before/after accelerated durability test (ADT) for Fe-N-RFC_C240. The electrode rotation speed was 1600 rpm in O_2-saturated 0.1 M KOH.

3.2.4 Carbon Pore Structure Effect on Active Site Formation

In order to verify the carbon pore structure effect on ORR active site formation, I investigated the ORR activity of Fe-N-C_CX series, which had been derived from pore-structure-engineered carbon supports. Interestingly, the catalyst samples were divided into two groups according to their onset potential region. For Fe-N-RFC_C30, C120, and C240, the onset potential was approx. 1.0 V and the difference among them started from the slope in the mixed kinetic-diffusion control region. However, Fe-N-RFC had its onset potential at approx. 0.9 V, a more negative potential that the others. It is worth mentioning that a high proportion of the micropore structure remained after Fe-N doping process in the former group, while it had completely disappeared in Fe-N-RFC (**Fig. 3.23b** and **Table 4**). Considering previous reports that the ORR catalytic active sites of Fe-N-C catalysts were hosted in the catalyst micropores, active sites might not be completely formed during heat treatment of the unactivated carbon template [74, 95]. This result indicated that the utilization of low microporous carbon supports might lead to poor performance of Fe-N-C catalysts.

In addition, the higher amounts of N incorporated during heat treatment in Fe-N-RFC_C30, C120, and C240 (0.94, 1.44, and 2.04 wt%, respectively) compared with that in Fe-N-RFC (0.20 wt%) indicated a higher chance of active site formation in the activated carbon templates. Especially, the amount of pyridinic N increased markedly compared with other N species when the samples were derived from carbon supports

with higher microporosities, as mentioned above. These linear correlations between the j_K values and pyridinic N contents were in accordance with previous reports of site features for active catalytic sites in pyrolyzed Fe-N-C catalysts, with the central Fe ion coordinated to four pyridinic-Ns attached to the edges of each graphene sheet. In other words, Fe-N_4 active sites could be formed in Fe-N-precursor-filled micropores of the RFC_CX carbon templates during heat treatment (**Fig 3.32**). Therefore, a higher active site density in the Fe-N-RFC_CXs was achieved with an increased micropore surface area in the initial RFC_CX templates. Considering the differences in PSD before and after the Fe and N doping process (**Fig 3.33**), mainly micropores between 1 and 2 nm were decreased in Fe-N-RFC_C30, C120, and C240, suggesting that the physical space required for Fe-N_4 sites to form on the edges of the two graphitic carbon surfaces could be strongly related to the specific micropore size of the carbon template, which seems to be around 1–2 nm. In addition, the mesopore size distribution in Fe-N-RFC_C240 was not much affected, strongly implying that the formation of Fe-N-C catalytic sites was not related to the mesopore regime. While the mesopore structures were ineffective to form the active site, the additional mesopores in Fe-N-RFC_C240 could enhance the mass transportation by smoothing the diffusion pathways and therefore increase the ORR activity.
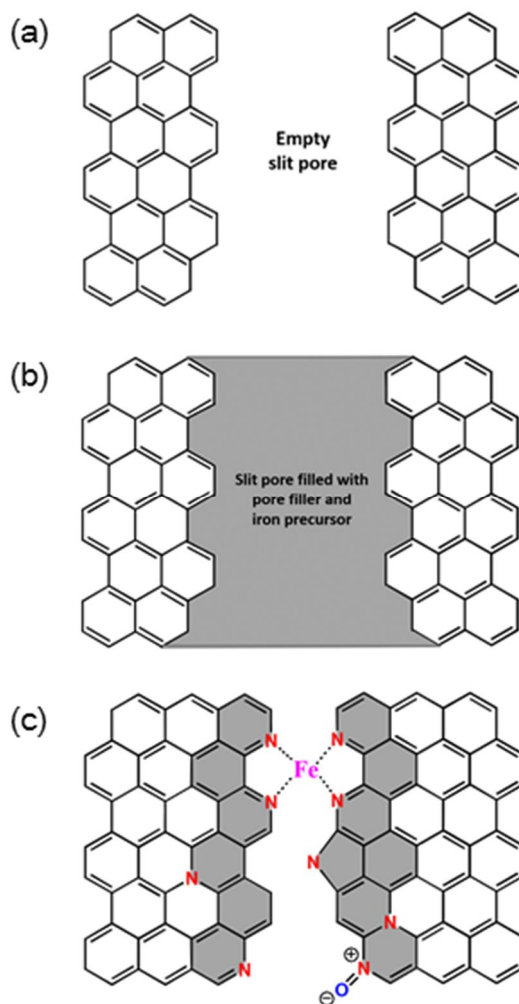
Figure 3.32. Illustration of Fe and N doping process within micropores:
Plan view of (a) an empty slit pore between two graphite edge surfaces after activation,
(b) a slit pore filled with pore filer and iron precursor after impregnation, and (c) the
presumed Fe and N configuration after Fe and N doping process. Shaded region
comes from pore filler.
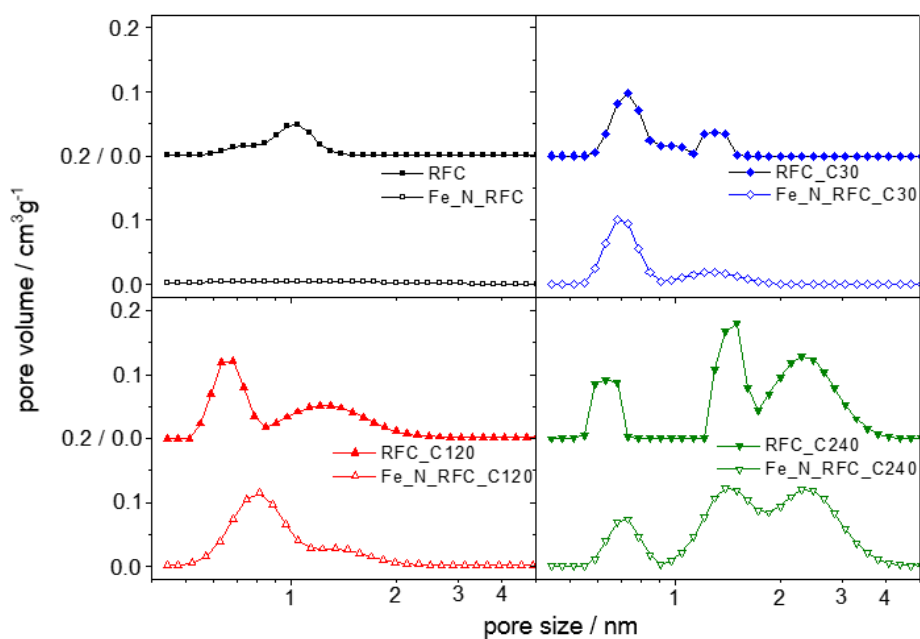
Figure 3.33. Pore structure change during Fe-N-doping process: comparative BET isotherm analyses on incremental pore volume as the function of pore size in samples before/after Fe-N-doping process.

Chapter 4. Conclusions

In this thesis, I verified two activity determining factors in Fe-N-C ORR catalyst synthetic process, which could improve the Fe-N$_4$ active site formation qualitatively and quantitatively. The first one is Fe-N coordination in precursors while the second is microporosity of carbon supports. The effects of these two factors on active site formation were confirmed by systematic precursor-controlled and carbon-support-controlled experiments, respectively.

First, the Fe-N coordination precursor effect on the active site formation was investigated with utilizing three phenanthroline isomers as N precursors. UV/Vis absorbance spectra of Fe-phenanthroline precursor solutions confirmed that only 1,10-phenanthroline formed coordination bonds with Fe while other two phenanthrolines didn't form, and TGA curves showed that the Fe-N coordination bonds with 1,10-phenanthroline suppressed the gasification of 1,10-phenathroline during high temperature pyrolysis, while 1,7-phenanthroline and 4,7-phenanthroline were completely gasified without Fe-N coordination. These different thermal behaviors of each precursor group led to different Fe and N configurations of resultant Fe-N-C catalysts. According to TEM and energy-filtered TEM analysis, Fe was evenly distributed with using 1,10-phenathroline, while Fe-related particles aggregated with 1,7-phenanthroline and 4,7-phenanthroline. XANES and EXAFS analysis further

demonstrated that Fe-N$_4$ active sites were well structured in Fe-N-C derived from 1,10-phenathroline, and that Fe$_3$O$_4$ particles were formed in those from 1,7-phenanthroline and 4,7-phenanthroline. Furthermore, the relative ratio of pyridinic N to graphitic N was significantly increased with using 1,10-phenathroline compared to others, implying that Fe-N coordination with 1,10-phenanthroline could have helped N-positioning for Fe-N$_4$ active site formation. Correspondingly, the Fe-N-C catalysts derived from 1,10-phenanthroline showed much superior ORR activity compared to the catalysts from other phenanthrolines, and there was a strong correlation between the relative ratio of pyridinic N to graphitic N and ORR kinetic current density, indicating that Fe-N coordination in precursor catalyzed Fe-N$_4$ active site formation during pyrolysis.

Next, the role of pre-defined microporosity of carbon supports in ORR catalytic site formation was investigated with the series of pore-controlled carbon supports. Before the Fe-N-C catalyst synthesis, spherical and monodisperse carbon supports were prepared and their pore structure were initially controlled by using hot CO_2 treatment. The development of porosity in these carbon supports was determined by nitrogen sorption isotherm measurements, and the enhanced micropore surface areas with CO_2 activation were further determined by the NLDFT (462, 903, 1536, and 2374 $m^2 \, g^{-1}$). After precursor impregnation and subsequent pyrolysis, Fe and N was successfully doped into these carbon supports. After Fe and N doping process, it was found that the

more developed microporosity in the parent carbon supports facilitates more Fe and N contents. Furthermore, XPS N1s spectra showed the relative portion of pyridinic N was selectively increased with increasing microporosity of initial carbon supports. Expectably, the higher microporosity of initial carbon supports actually led to more ORR active Fe-N-C catalysts, and a strong correlation was found between N contents, especially pyridinic N, and ORR kinetic current density. This results suggested that the enlarged microporosity of carbon supports contributed to the increase of Fe-N$_4$ active site density during pyrolysis.

From the above precursor and carbon support study, Fe-N coordination in precursors and microporosity of carbon supports were indeed demonstrated to be ORR activity determining factors. During pyrolysis, the Fe-N coordination could boost the Fe-N$_4$ active site formation and micropores could offer the spots for developing those active sites. Through proper adjustment and convergence of two factors proposed in this thesis, it is expected that a synthesis design for optimal Fe-N-C catalysts could be devised near future.

References

1.   F. Barbir. "*PEM fuel cells: theory and practice*". Academic Press (2012).

2.   R. von Helmolt, U. Eberle. "Fuel cell vehicles: Status 2007". *Journal of Power Sources* **165**, 833-843 (2007).

3.   M. Winter, R.J. Brodd. "What Are Batteries, Fuel Cells, and Supercapacitors?". *Chemical Reviews* **104**, 4245-4270 (2004).

4.   J. Zhang. "*PEM fuel cell electrocatalysts and catalyst layers: fundamentals and applications*". Springer Science & Business Media (2008).

5.   J. Larminie, A. Dicks, M.S. McDonald. "*Fuel cell systems explained*". J. Wiley Chichester, UK (2003).

6.   A. Appleby. "From Sir William Grove to today: fuel cells and the future". *Journal of Power Sources* **29**, 3-11 (1990).

7.   R. O'hayre, S.-W. Cha, F.B. Prinz, W. Colella. "*Fuel cell fundamentals*". John Wiley & Sons (2016).

8.   R. Borup, J. Meyers, B. Pivovar, Y.S. Kim, R. Mukundan, N. Garland, D. Myers, M. Wilson, F. Garzon, D. Wood. "Scientific aspects of polymer

electrolyte fuel cell durability and degradation". *Chemical reviews* **107**, 3904-3951 (2007).

9. G. Frenette, D. Forthoffer. "Economic & commercial viability of hydrogen fuel cell vehicles from an automotive manufacturer perspective". *International Journal of Hydrogen Energy* **34**, 3578-3588 (2009).

10. M. Granovskii, I. Dincer, M.A. Rosen. "Economic and environmental comparison of conventional, hybrid, electric and hydrogen fuel cell vehicles". *Journal of Power Sources* **159**, 1186-1193 (2006).

11. DOE Hydrogen and Fuel Cells Program. "The Department of Energy Hydrogen and Fuel Cells Program Plan". *U.S. Department of Energy* (2011).

12. M.K. Debe, A.K. Schmoeckel, G.D. Vernstrom, R. Atanasoski. "High voltage stability of nanostructured thin film catalysts for PEM fuel cells". *Journal of Power Sources* **161**, 1002-1011 (2006).

13. L. Gancs, T. Kobayashi, M.K. Debe, R. Atanasoski, A. Wieckowski. "Crystallographic characteristics of nanostructured thin-film fuel cell electrocatalysts: A HRTEM study". *Chemistry of Materials* **20**, 2444-2454 (2008).

14. F. Jaouen, E. Proietti, M. Lefèvre, R. Chenitz, J.-P. Dodelet, G. Wu, H.T. Chung, C.M. Johnston, P. Zelenay. "Recent advances in non-precious metal catalysis for oxygen-reduction reaction in polymer electrolyte fuel cells". *Energy & Environmental Science* **4**, 114-130 (2011).

15. W. Liu, D. Zuckerbrod. "In situ detection of hydrogen peroxide in PEM fuel cells". *Journal of The Electrochemical Society* **152**, A1165-A1170 (2005).

16. X. Ren, P. Zelenay, S. Thomas, J. Davey, S. Gottesfeld. "Recent advances in direct methanol fuel cells at Los Alamos National Laboratory". *Journal of Power Sources* **86**, 111-116 (2000).

17. V.R. Stamenkovic, B. Fowler, B.S. Mun, G. Wang, P.N. Ross, C.A. Lucas, N.M. Marković. "Improved oxygen reduction activity on Pt3Ni (111) via increased surface site availability". *science* **315**, 493-497 (2007).

18. R. Subbaraman, D. Strmcnik, A.P. Paulikas, V.R. Stamenkovic, N.M. Markovic. "Oxygen Reduction Reaction at Three-Phase Interfaces". *ChemPhysChem* **11**, 2825-2833 (2010).

19. K. Kreuer. "On the development of proton conducting polymer membranes for hydrogen and methanol fuel cells". *Journal of membrane science* **185**, 29-39 (2001).

20. H.K. Atiyeh, K. Karan, B. Peppley, A. Phoenix, E. Halliop, J. Pharoah. "Experimental investigation of the role of a microporous layer on the water transport and performance of a PEM fuel cell". *Journal of Power Sources* **170**, 111-121 (2007).

21. P. Costamagna, S. Srinivasan. "Quantum jumps in the PEMFC science and technology from the 1960s to the year 2000: Part II. Engineering, technology development and application aspects". *Journal of power sources* **102**, 253-269 (2001).

22. L. Cindrella, A. Kannan, J. Lin, K. Saminathan, Y. Ho, C. Lin, J. Wertz. "Gas diffusion layer for proton exchange membrane fuel cells—A review". *Journal of Power Sources* **194**, 146-160 (2009).

23. S.M. Haile. "Fuel cell materials and components". *Acta Materialia* **51**, 5981-6000 (2003).

24. J.K. Nørskov, J. Rossmeisl, A. Logadottir, L. Lindqvist, J.R. Kitchin, T. Bligaard, H. Jonsson. "Origin of the overpotential for oxygen reduction at a fuel-cell cathode". *The Journal of Physical Chemistry B* **108**, 17886-17892 (2004).

25. Z. Chen, J.-P. Dodelet, J. Zhang. "*Non-noble metal fuel cell catalysts*". John Wiley & Sons (2014).

26. H.A. Gasteiger, S.S. Kocha, B. Sompalli, F.T. Wagner. "Activity benchmarks and requirements for Pt, Pt-alloy, and non-Pt oxygen reduction catalysts for PEMFCs". *Applied Catalysis B: Environmental* **56**, 9-35 (2005).

27. U. Paulus, A. Wokaun, G. Scherer, T. Schmidt, V. Stamenkovic, N.M. Markovic, P. Ross. "Oxygen reduction on high surface area Pt-based alloy catalysts in comparison to well defined smooth bulk alloy electrodes". *Electrochimica Acta* **47**, 3787-3798 (2002).

28. U. Paulus, A. Wokaun, G. Scherer, T. Schmidt, V. Stamenkovic, V. Radmilovic, N. Markovic, P. Ross. "Oxygen reduction on carbon-supported Pt−Ni and Pt−Co alloy catalysts". *The Journal of Physical Chemistry B* **106**, 4181-4191 (2002).

29. E. Antolini, J.R. Salgado, E.R. Gonzalez. "The stability of Pt–M (M= first row transition metal) alloy catalysts and its effect on the activity in low temperature fuel cells: a literature review and tests on a Pt–Co catalyst". *Journal of Power Sources* **160**, 957-968 (2006).

30. X. Yu, S. Ye. "Recent advances in activity and durability enhancement of Pt/C catalytic cathode in PEMFC: Part II: Degradation mechanism and durability enhancement of carbon supported platinum catalyst". *Journal of Power Sources* **172**, 145-154 (2007).

31. S. Chen, J. Bi, Y. Zhao, L. Yang, C. Zhang, Y. Ma, Q. Wu, X. Wang, Z. Hu. "Nitrogen-Doped Carbon Nanocages as Efficient Metal-Free Electrocatalysts for Oxygen Reduction Reaction". *Advanced materials* **24**, 5593-5597 (2012).

32. K. Gong, F. Du, Z. Xia, M. Durstock, L. Dai. "Nitrogen-doped carbon nanotube arrays with high electrocatalytic activity for oxygen reduction". *science* **323**, 760-764 (2009).

33. L. Yang, S. Jiang, Y. Zhao, L. Zhu, S. Chen, X. Wang, Q. Wu, J. Ma, Y. Ma, Z. Hu. "Boron-doped carbon nanotubes as metal-free electrocatalysts for the oxygen reduction reaction". *Angewandte Chemie* **123**, 7270-7273 (2011).

34. S. Yang, L. Zhi, K. Tang, X. Feng, J. Maier, K. Müllen. "Efficient synthesis of heteroatom (N or S)-doped graphene based on ultrathin graphene oxide-porous silica sheets for oxygen reduction reactions". *Advanced Functional Materials* **22**, 3634-3640 (2012).

35. M. Lefèvre, E. Proietti, F. Jaouen, J.-P. Dodelet. "Iron-based catalysts with improved oxygen reduction activity in polymer electrolyte fuel cells". *science* **324**, 71-74 (2009).

36. E. Proietti, F. Jaouen, M. Lefèvre, N. Larouche, J. Tian, J. Herranz, J.-P. Dodelet. "Iron-based cathode catalyst with enhanced power density in polymer electrolyte membrane fuel cells". *Nature communications* **2**, 416

(2011).

37.   J. Shui, C. Chen, L. Grabstanowicz, D. Zhao, D.-J. Liu. "Highly efficient nonprecious metal catalyst prepared with metal–organic framework in a continuous carbon nanofibrous network". *Proceedings of the National Academy of Sciences* **112**, 10629-10634 (2015).

38.   G. Wu, K.L. More, C.M. Johnston, P. Zelenay. "High-performance electrocatalysts for oxygen reduction derived from polyaniline, iron, and cobalt". *Science* **332**, 443-447 (2011).

39.   Y. Feng, A. Gago, L. Timperman, N. Alonso-Vante. "Chalcogenide metal centers for oxygen reduction reaction: activity and tolerance". *Electrochimica Acta* **56**, 1009-1022 (2011).

40.   M.R. Gao, J. Jiang, S.H. Yu. "Solution-Based Synthesis and Design of Late Transition Metal Chalcogenide Materials for Oxygen Reduction Reaction (ORR)". *Small* **8**, 13-27 (2012).

41.   M.-R. Gao, Y.-F. Xu, J. Jiang, S.-H. Yu. "Nanostructured metal chalcogenides: synthesis, modification, and applications in energy conversion and storage devices". *Chemical Society Reviews* **42**, 2986-3017 (2013).

42.   A. Lewera, J. Inukai, W. Zhou, D. Cao, H. Duong, N. Alonso-Vante, A. Wieckowski. "Chalcogenide oxygen reduction reaction catalysis: X-ray photoelectron spectroscopy with Ru, Ru/Se and Ru/S samples emersed from aqueous media". *Electrochimica Acta* **52**, 5759-5765 (2007).

43.   A. Ishihara, Y. Ohgi, K. Matsuzawa, S. Mitsushima, K.-i. Ota. "Progress in non-precious metal oxide-based cathode for polymer electrolyte fuel cells".

Electrochimica Acta **55**, 8005-8012 (2010).

44. Y. Liang, Y. Li, H. Wang, J. Zhou, J. Wang, T. Regier, H. Dai. "Co3O4 nanocrystals on graphene as a synergistic catalyst for oxygen reduction reaction". *Nature materials* **10**, 780-786 (2011).

45. I. Roche, E. Chaînet, M. Chatenet, J. Vondrák. "Carbon-supported manganese oxide nanoparticles as electrocatalysts for the oxygen reduction reaction (ORR) in alkaline medium: physical characterizations and ORR mechanism". *The Journal of Physical Chemistry C* **111**, 1434-1443 (2007).

46. J. Suntivich, H.A. Gasteiger, N. Yabuuchi, H. Nakanishi, J.B. Goodenough, Y. Shao-Horn. "Design principles for oxygen-reduction activity on perovskite oxide catalysts for fuel cells and metal–air batteries". *Nature chemistry* **3**, 546-550 (2011).

47. R. Jasinski. "A new fuel cell cathode catalyst". (1964).

48. V. Bagotzky, M. Tarasevich, K. Radyushkina, O. Levina, S. Andrusyova. "Electrocatalysis of the oxygen reduction process on metal chelates in acid electrolyte". *Journal of Power Sources* **2**, 233-240 (1978).

49. S. Gupta, D. Tryk, I. Bae, W. Aldred, E. Yeager. "Heat-treated polyacrylonitrile-based catalysts for oxygen electroreduction". *Journal of applied electrochemistry* **19**, 19-27 (1989).

50. Z.-F. Ma, X.-Y. Xie, X.-X. Ma, D.-Y. Zhang, Q. Ren, N. Heß-Mohr, V.M. Schmidt. "Electrochemical characteristics and performance of CoTMPP/BP oxygen reduction electrocatalysts for PEM fuel cell". *Electrochemistry communications* **8**, 389-394 (2006).

51.   J. Van Veen, H. Colijn. "Oxygen Reduction on Transition-Metal Porphyrins in Acid Electrolyte II. Stability". *Berichte der Bunsengesellschaft für physikalische Chemie* **85**, 700-704 (1981).

52.   J. Van Veen, J. Van Baar, C. Kroese, J. Coolegem, N. De Wit, H. Colijn. "Oxygen Reduction on Transition-Metal Porphyrins in Acid Electrolyte I. Activity". *Berichte der Bunsengesellschaft für physikalische Chemie* **85**, 693-700 (1981).

53.   A. Garsuch, R. d'Eon, T. Dahn, O. Klepel, R.R. Garsuch, J.R. Dahn. "Oxygen reduction behavior of highly porous non-noble metal catalysts prepared by a template-assisted synthesis route". *Journal of The Electrochemical Society* **155**, B236-B243 (2008).

54.   H. Liu, Z. Shi, J. Zhang, L. Zhang, J. Zhang. "Ultrasonic spray pyrolyzed iron-polypyrrole mesoporous spheres for fuel celloxygen reduction electrocatalysts". *Journal of Materials Chemistry* **19**, 468-470 (2009).

55.   A. Serov, M.H. Robson, M. Smolnik, P. Atanassov. "Templated bi-metallic non-PGM catalysts for oxygen reduction". *Electrochimica Acta* **80**, 213-218 (2012).

56.   P. Bogdanoff, I. Herrmann, M. Hilgendorff, I. Dorbandt, S. Fiechter, H. Tributsch. "Probing structural effects of pyrolysed CoTMPP-based electrocatalysts for oxygen reduction via new preparation strategies". *Journal of new materials for electrochemical systems* **7**, 85-92 (2004).

57.   I. Herrmann, U. Kramm, S. Fiechter, P. Bogdanoff. "Oxalate supported pyrolysis of CoTMPP as electrocatalysts for the oxygen reduction reaction".

Electrochimica Acta **54**, 4275-4287 (2009).

58.   M. Bron, S. Fiechter, M. Hilgendorff, P. Bogdanoff. "Catalysts for oxygen reduction from heat-treated carbon-supported iron phenantroline complexes". *Journal of applied electrochemistry* **32**, 211-216 (2002).

59.   M. Bron, J. Radnik, M. Fieber-Erdmann, P. Bogdanoff, S. Fiechter. "EXAFS, XPS and electrochemical studies on oxygen reduction catalysts obtained by heat treatment of iron phenanthroline complexes supported on high surface area carbon black". *Journal of Electroanalytical Chemistry* **535**, 113-119 (2002).

60.   J. Tian, L. Birry, F. Jaouen, J.P. Dodelet. "Fe-based catalysts for oxygen reduction in proton exchange membrane fuel cells with cyanamide as nitrogen precursor and/or pore-filler". *Electrochimica Acta* **56**, 3276-3285 (2011).

61.   G. Liu, X. Li, P. Ganesan, B.N. Popov. "Studies of oxygen reduction reaction active sites and stability of nitrogen-modified carbon composite catalysts for PEM fuel cells". *Electrochimica Acta* **55**, 2853-2858 (2010).

62.   M. Ferrandon, A.J. Kropf, D.J. Myers, K. Artyushkova, U. Kramm, P. Bogdanoff, G. Wu, C.M. Johnston, P. Zelenay. "Multitechnique characterization of a polyaniline–iron–carbon oxygen reduction catalyst". *The Journal of Physical Chemistry C* **116**, 16001-16013 (2012).

63.   T.E. Wood, Z. Tan, A.K. Schmoeckel, D. O'Neill, R. Atanasoski. "Non-precious metal oxygen reduction catalyst for PEM fuel cells based on nitroaniline precursor". *Journal of Power Sources* **178**, 510-516 (2008).

64. G. Wu, K. Artyushkova, M. Ferrandon, A.J. Kropf, D. Myers, P. Zelenay. "Performance durability of polyaniline-derived non-precious cathode catalysts". *ECS Transactions* **25**, 1299-1311 (2009).

65. J. Fournier, G. Lalande, D. Guay, J.P. Dodelet. "Activation of Various Fe-Based Precursors on Carbon Black and Graphite Supports to Obtain Catalysts for the Reduction of Oxygen in Fuel Cells". *Journal of The Electrochemical Society* **144**, 218-226 (1997).

66. F. Jaouen, F. Charreteur, J. Dodelet. "Fe-based catalysts for oxygen reduction in PEMFCS importance of the disordered phase of the carbon support". *Journal of the Electrochemical Society* **153**, A689-A698 (2006).

67. F. Jaouen, S. Marcotte, J.-P. Dodelet, G. Lindbergh. "Oxygen reduction catalysts for polymer electrolyte fuel cells from the pyrolysis of iron acetate adsorbed on various carbon supports". *The Journal of Physical Chemistry B* **107**, 1376-1386 (2003).

68. G. Lalande, D. Guay, J. Dodelet, G. Denes. "Influence of Nitrogen-Containing Precursors on the Electrocatalytic Activity of Heat-Treated Fe (OH) 2 on Carbon Black for O 2 Reduction". *Journal of the Electrochemical Society* **145**, 2411-2418 (1998).

69. G. Goenaga, S. Ma, S. Yuan, D.-J. Liu. "New approaches to non-PGM electrocatalysts using porous framework materials". *ECS Transactions* **33**, 579-586 (2010).

70. M. Lefèvre, J.-P. Dodelet. "Recent advances in non-precious metal electrocatalysts for oxygen reduction in PEM fuel cells". *Ecs Transactions* **45**, 35-44 (2012).

71. D. Zhao, J.-L. Shui, C. Chen, X. Chen, B.M. Reprogle, D. Wang, D.-J. Liu. "Iron imidazolate framework as precursor for electrocatalysts in polymer electrolyte membrane fuel cells". *Chemical Science* **3**, 3200-3205 (2012).

72. A. Bouwkamp-Wijnoltz, W. Visscher, J. Van Veen, E. Boellaard, A. Van der Kraan, S. Tang. "On active-site heterogeneity in pyrolyzed carbon-supported iron porphyrin catalysts for the electrochemical reduction of oxygen: an in situ mössbauer study". *The Journal of Physical Chemistry B* **106**, 12993-13001 (2002).

73. G. Faubert, R. Côté, D. Guay, J.P. Dodelet, G. Dénès, C. Poleunis, P. Bertrand. "Activation and characterization of Fe-based catalysts for the reduction of oxygen in polymer electrolyte fuel cells". *Electrochimica Acta* **43**, 1969-1984 (1998).

74. F. Jaouen, J. Herranz, M. Lefevre, J.-P. Dodelet, U.I. Kramm, I. Herrmann, P. Bogdanoff, J. Maruyama, T. Nagaoka, A. Garsuch. "Cross-laboratory experimental study of non-noble-metal electrocatalysts for the oxygen reduction reaction". *ACS applied materials & interfaces* **1**, 1623-1639 (2009).

75. Q. Jia, N. Ramaswamy, H. Hafiz, U. Tylus, K. Strickland, G. Wu, B. Barbiellini, A. Bansil, E.F. Holby, P. Zelenay. "Experimental observation of redox-induced Fe–N switching behavior as a determinant role for oxygen reduction activity". *ACS nano* **9**, 12496-12505 (2015).

76. U.I. Koslowski, I. Abs-Wurmbach, S. Fiechter, P. Bogdanoff. "Nature of the catalytic centers of porphyrin-based electrocatalysts for the ORR: a correlation of kinetic current density with the site density of Fe$-$N4 centers". *The Journal of Physical Chemistry C* **112**, 15356-15366 (2008).

77. U.I. Kramm, J. Herranz, N. Larouche, T.M. Arruda, M. Lefèvre, F. Jaouen, P. Bogdanoff, S. Fiechter, I. Abs-Wurmbach, S. Mukerjee. "Structure of the catalytic sites in Fe/N/C-catalysts for O 2-reduction in PEM fuel cells". *Physical Chemistry Chemical Physics* **14**, 11673-11688 (2012).

78. U.I. Kramm, M. Lefèvre, N. Larouche, D. Schmeisser, J.-P. Dodelet. "Correlations between Mass Activity and Physicochemical Properties of Fe/N/C Catalysts for the ORR in PEM Fuel Cell via 57Fe Mössbauer Spectroscopy and Other Techniques". *Journal of the American Chemical Society* **136**, 978-985 (2014).

79. G. Lalande, G. Faubert, R. Cote, D. Guay, J. Dodelet, L. Weng, P. Bertrand. "Catalytic activity and stability of heat-treated iron phthalocyanines for the electroreduction of oxygen in polymer electrolyte fuel cells". *Journal of power sources* **61**, 227-237 (1996).

80. M. Lefèvre, J. Dodelet, P. Bertrand. "Molecular oxygen reduction in PEM fuel cells: evidence for the simultaneous presence of two active sites in Fe-based catalysts". *The Journal of Physical Chemistry B* **106**, 8705-8713 (2002).

81. J. Li, S. Ghoshal, W. Liang, M.-T. Sougrati, F. Jaouen, B. Halevi, S. McKinney, G. McCool, C. Ma, X. Yuan. "Structural and mechanistic basis for the high activity of Fe–N–C catalysts toward oxygen reduction". *Energy & Environmental Science* **9**, 2418-2432 (2016).

82. J. Maruyama, I. Abe. "Fuel cell cathode catalyst with heme-like structure formed from nitrogen of glycine and iron". *Journal of the Electrochemical Society* **154**, B297-B304 (2007).

83.   H. Schulenburg, S. Stankov, V. Schünemann, J. Radnik, I. Dorbandt, S. Fiechter, P. Bogdanoff, H. Tributsch. "Catalysts for the oxygen reduction from heat-treated iron (III) tetramethoxyphenylporphyrin chloride: structure and stability of active sites". *The Journal of Physical Chemistry B* **107**, 9034-9041 (2003).

84.   U.I. Kramm, I. Herrmann-Geppert, J. Behrends, K. Lips, S. Fiechter, P. Bogdanoff. "On an easy way to prepare metal–nitrogen doped carbon with exclusive presence of MeN4-type sites active for the ORR". *Journal of the American Chemical Society* **138**, 635-640 (2016).

85.   Y.J. Sa, D.-J. Seo, J. Woo, J.T. Lim, J.Y. Cheon, S.Y. Yang, J.M. Lee, D. Kang, T.J. Shin, H.S. Shin. "A General Approach to Preferential Formation of Active Fe–N x Sites in Fe–N/C Electrocatalysts for Efficient Oxygen Reduction Reaction". *Journal of the American Chemical Society* **138**, 15046-15056 (2016).

86.   N.R. Sahraie, U.I. Kramm, J. Steinberg, Y. Zhang, A. Thomas, T. Reier, J.-P. Paraknowitsch, P. Strasser. "Quantifying the density and utilization of active sites in non-precious metal oxygen electroreduction catalysts". *Nature communications* **6**, 8618 (2015).

87.   J. Tian, A. Morozan, M.T. Sougrati, M. Lefèvre, R. Chenitz, J.P. Dodelet, D. Jones, F. Jaouen. "Optimized synthesis of Fe/N/C cathode catalysts for PEM fuel cells: a matter of iron–ligand coordination strength". *Angewandte Chemie* **125**, 7005-7008 (2013).

88.   C.W. Bezerra, L. Zhang, K. Lee, H. Liu, J. Zhang, Z. Shi, A.L. Marques, E.P. Marques, S. Wu, J. Zhang. "Novel carbon-supported Fe-N electrocatalysts

synthesized through heat treatment of iron tripyridyl triazine complexes for the PEM fuel cell oxygen reduction reaction". *Electrochimica Acta* **53**, 7703-7710 (2008).

89.   S. Liu, C. Deng, L. Yao, H. Zhong, H. Zhang. "Synthesis highly active and durable non-precious-metal catalyst with 2, 2-pyridylbenzimidazole as novel nitrogen coordination compound for oxygen reduction reaction". *Catalysis Communications* **58**, 112-116 (2015).

90.   A. Velázquez-Palenzuela, L. Zhang, L. Wang, P.L. Cabot, E. Brillas, K. Tsay, J. Zhang. "Carbon-Supported Fe–N x Catalysts Synthesized by Pyrolysis of the Fe (II)–2, 3, 5, 6-Tetra (2-pyridyl) pyrazine Complex: Structure, Electrochemical Properties, and Oxygen Reduction Reaction Activity". *The Journal of Physical Chemistry C* **115**, 12929-12940 (2011).

91.   G. Wang, K. Jiang, M. Xu, C. Min, B. Ma, X. Yang. "A high activity nitrogen-doped carbon catalyst for oxygen reduction reaction derived from polyaniline-iron coordination polymer". *Journal of Power Sources* **266**, 222-225 (2014).

92.   L. Wang, L. Zhang, J. Zhang. "Improved ORR activity of non-noble metal electrocatalysts by increasing ligand and metal ratio in synthetic complex precursors". *Electrochimica Acta* **56**, 5488-5492 (2011).

93.   J. Wu, W. Li, D. Higgins, Z. Chen. "Heat-treated nonprecious catalyst using Fe and nitrogen-rich 2, 3, 7, 8-tetra (pyridin-2-yl) pyrazino [2, 3-g] quinoxaline coordinated complex for oxygen reduction reaction in PEM fuel cells". *The Journal of Physical Chemistry C* **115**, 18856-18862 (2011).

94.   Y. Zhao, K. Kamiya, K. Hashimoto, S. Nakanishi. "Efficient oxygen

reduction reaction electrocatalysts synthesized from an iron-coordinated aromatic polymer framework". *Journal of Materials Chemistry A* **4**, 3858-3864 (2016).

95.   F. Jaouen, M. Lefèvre, J.-P. Dodelet, M. Cai. "Heat-treated Fe/N/C catalysts for O2 electroreduction: are active sites hosted in micropores?". *The Journal of Physical Chemistry B* **110**, 5553-5558 (2006).

96.   J.-Y. Choi, R.S. Hsu, Z. Chen. "Highly active porous carbon-supported nonprecious metal− N electrocatalyst for oxygen reduction reaction in PEM fuel cells". *The Journal of Physical Chemistry C* **114**, 8048-8053 (2010).

97.   A.E. Harvey, J.A. Smart, E.S. Amis. "Simultaneous Spectrophotometric Determination of Iron(II) and Total Iron with 1,10-Phenanthroline". *Analytical Chemistry* **27**, 26-29 (1955).

98.   Mudasir, N. Yoshioka, H. Inoue. "DNA binding of iron(II) mixed-ligand complexes containing 1,10-phenanthroline and 4,7-diphenyl-1,10-phenanthroline". *Journal of Inorganic Biochemistry* **77**, 239-247 (1999).

99.   M.E.F. Brollo, R. López-Ruiz, D. Muraca, S.J. Figueroa, K.R. Pirota, M. Knobel. "Compact Ag@ Fe3O4 Core-shell Nanoparticles by Means of Single-step Thermal Decomposition Reaction". *Scientific reports* **4**,   (2014).

100.   A. Zitolo, V. Goellner, V. Armel, M.-T. Sougrati, T. Mineva, L. Stievano, E. Fonda, F. Jaouen. "Identification of catalytic sites for oxygen reduction in iron-and nitrogen-doped graphene materials". *Nature materials* **14**, 937-942 (2015).

101.   A.J. Bard, L.R. Faulkner, J. Leddy, C.G. Zoski. "*Electrochemical methods:*

fundamentals and applications". Wiley New York (1980).

102. U. Tylus, Q. Jia, K. Strickland, N. Ramaswamy, A. Serov, P. Atanassov, S. Mukerjee. "Elucidating oxygen reduction active sites in pyrolyzed metal–nitrogen coordinated non-precious-metal electrocatalyst systems". *The Journal of Physical Chemistry C* **118**, 8999-9008 (2014).

103. H.S. Kim, M.S. Kang, W.C. Yoo. "Highly Enhanced Gas Sorption Capacities of N-Doped Porous Carbon Spheres by Hot NH3 and CO2 Treatments". *The Journal of Physical Chemistry C* **119**, 28512-28522 (2015).

104. W.C. Yoo, A. Stein. "Solvent effects on morphologies of mesoporous silica spheres prepared by pseudomorphic transformations". *Chemistry of Materials* **23**, 1761-1767 (2011).

105. A. Ōya, H. Marsh. "Phenomena of catalytic graphitization". *Journal of Materials Science* **17**, 309-322 (1982).

106. S. Gupta, C. Fierro, E. Yeager. "The effects of cyanide on the electrochemical properties of transition metal macrocycles for oxygen reduction in alkaline solutions". *Journal of electroanalytical chemistry and interfacial electrochemistry* **306**, 239-250 (1991).

107. S. Lee, D.-H. Kwak, S.-B. Han, Y.-W. Lee, J.-Y. Lee, I.-A. Choi, H.-S. Park, J.-Y. Park, K.-W. Park. "Bimodal Porous Iron/Nitrogen-Doped Highly Crystalline Carbon Nanostructure as a Cathode Catalyst for the Oxygen Reduction Reaction in an Acid Medium". *ACS Catalysis* **6**, 5095-5102 (2016).

국문초록

철−질소−탄소 촉매 내 산소 환원 반응
활성점 형성의 최적화를 위한 합성 설계

고분자 전해질 연료전지는 수소와 산소의 화학적 에너지를 전기 에너지로

변환시켜주는 에너지 변환장치로써, 에너지 변환 효율이 높고 부산물로

공해 물질 없이 물만 배출하여 친환경 차세대 에너지 소자로 주목 받고

있다. 고분자 전해질 연료전지는 환원극에서의 느린 산소 환원 반응으로

인하여 전기화학 촉매를 필요로 하는데, 현재에는 백금 소재의 촉매가 상

용적으로 사용되고 있다. 하지만 비싼 가격과 희소성으로 인하여 백금을

촉매 재료로 사용하는 것은 고분자 전해질 막 연료전지의 상용화에 대한

걸림돌로 작용하고 있다. 따라서 백금을 대체할 차세대 촉매 물질에 대한

연구의 진행이 활발하게 이루어지고 있다. 비백금계 촉매로는 금속 산화

물, 금속−질소−탄소 복합체 촉매, 질소−탄소 복합체 촉매 등이 연구되

고 있으며, 이 중에서도 철−질소−탄소 촉매들이 가장 우수한 성능을 보

고하고 있다. 이러한 철−질소−탄소 촉매들은 일반적으로 철, 질소, 탄소

전구체의 혼합물을 고온에서 열처리함으로써 합성할 수 있다. 최근의 분광학 연구 결과들을 종합하여 보면, 철-질소-탄소 촉매의 활성점은 탄소의 미소 기공 내에 형성된 철-질소 배위 구조에 기반하고 있음을 알 수 있다. 하지만, 이러한 활성점을 형성하기 위한 포괄적인 합성 방법 혹은 가이드 라인은 아직 확립되지 못한 상황이다. 이에 본 연구에서는 체계적인 실험을 통해 철-질소-탄소 촉매 합성에 대한 전구체 및 탄소 담지체의 효과를 조사하고, 이를 통해 철-질소 활성점 형성의 최적화를 위한 합리적인 합성 설계를 제안하고자 하였다.

먼저 전구체 상태에서의 배위 결합의 유무가 철-질소-탄소 촉매에서의 활성점 형성에 미치는 영향을 확인하는 실험을 진행하였다. 질소의 치환 위치에 따른 구조 이성질체를 갖는 페난트롤린들을 질소 전구체로 사용할 때, 1,10-페난트롤린만이 철과 배위 결합을 하고, 1,7-페난트롤린과 4,7-페난트롤린은 배위 결합을 하지 않는 것이 자외선 가시광 흡수 분광법을 통해 확인할 수 있었다. 이 전구체들을 통하여 철-질소-탄소 촉매를 합성하였을 때, 배위 결합을 한 1,10-페난트롤린을 사용한 것이 산소 환원 반응 성능이 월등히 높았다. 투과 전자 현미경 및 엑스선 회절 분석을 통해 확인한 결과, 배위 결합을 한 전구체를 사용한 것은 철이 원자 단위로 잘 분산되어 있는 반면에 배위 결합을 하지 않은 전구체를 사

용한 것은 철이 덩어리로 뭉치는 것을 확인하였다. 또한, 엑스선 광전자 분광법을 통해 분석한 결과, 배위 결합을 한 전구체를 사용한 경우에 피리디닉 질소의 비율이 크게 증가한 것을 확인하였다. 이를 통해 전구체내 배위 결합의 존재가 형성된 활성점의 질적 향상을 이루었음을 알 수 있었다.

다음으로 탄소 담지체의 기공 구조가 철−질소−탄소 촉매의 활성점 형성에 어떠한 영향을 미치는지를 확인하는 실험을 진행하였다. 이산화탄소 활성화 처리 시간으로 기공 구조가 조절된 탄소 담지체에, 동일한 양의 철과 질소 전구체를 함침한 후에 고온 열처리를 통해 촉매를 합성한 결과, 미소 기공률이 더 발달한 탄소 담지체를 사용한 경우에 철과 질소의 함량, 특히 피리디닉 질소의 비율이 더 커진 것을 확인할 수 있었다. 또한, 산소 환원 반응 활성 역시 미소 기공률이 발달한 탄소 담지체를 통해 만든 촉매가 더 높은 것을 확인하였다. 이를 통해서, 탄소 담지체의 미소 기공률이 높을수록 만들어진 촉매의 활성점의 양적 향상이 이루어졌음을 알 수 있었다.

위 두 가지 실험을 종합하여 볼 때, 전구체내 배위 결합 형성을 통해 활성점의 질적 향상을, 탄소 담지체의 미소 기공률 증대를 통한 활성점의 양적 향상을 가져올 수 있음을 확인할 수 있다. 본 연구의 결과를 바탕으

122

로 철−질소−탄소 촉매에 대한 합리적인 합성 설계를 구상할 수 있을 것이며, 최적의 성능을 갖는 철−질소−탄소 촉매를 실제로 합성하는 데에도 도움이 될 것으로 기대한다.

List of Publications (SCI)

1st or co-1st author

1. **Minhyoung Kim**, Yun Sik Kang, Jee Yun Park, Sang Kown Yoon and Yung-Eun Sung, "Metal-coated Polyether Ether Ketone Monopolar Plates for Polymer Electrolyte Membrane Fuel Cell" *Bulletin of the Korean Chemical Society,* **36**, 2815 (2015)

2. Segeun Jang, **Minhyoung Kim**, Yun Sik Kang, Yong Whan Choi, Sang Moon Kim, Yung-Eun Sung and Mansoo Choi, "Facile Multiscale Patterning by Creep-Assisted Sequential Imprinting and Fuel Cell Application", *ACS Applied Materials & Interfaces,* **8**, 11459 (2016)

3. **Minhyoung Kim**, Hee Soo Kim, Sung Jong Yoo, Won Cheol Yoo, Yung-Eun Sung, "The role of pre-defined microporosity in catalytic site formation for the oxygen reduction reaction in iron- and nitrogen-doped carbon materials", *Journal of Materials Chemistry A,* **5**, 4199 (2017)

Co-author

1. Ju Wan Lim, Yong-Hun Cho, Minjeh Ahn, Dong Young Chung, Yoon-Hwan Cho, Namgee Jung, Yun Sik Kang, Ok-Hee Kim, Myeong Jae Lee,

Minhyoung Kim, Yung-Eun Sung, "Ionic Resistance of a Cathode Catalyst Layer with Various Thicknesses by Electrochemical Impedance Spectroscopy for PEMFC" *Journal of the Electrochemical Society*, **159**, B378 (2012)

2. Ok-Hee Kim, Yong-Hun Cho, Soon Hyung Kang, Hee-Young Park, Minhyoung Kim, Ju Wan Lim, Dong Young Chung, Myeong Jae Lee, Heeman Choe, Yung-Eun Sung, "Ordered macroporous platinum electrode and enhanced mass transfer in fuel cells using inverse opal structure", *Nature Communications,* **4**, 2473 (2013)

3. Hyelim Choi, Ok-Hee Kim, Minhyoung Kim, Heeman Choe, Yong-Hun Cho, and Yung-Eun Sung, "Next-Generation Polymer-Electrolyte-Membrane Fuel Cells Using Titanium Foam as Gas Diffusion Layer", *ACS Applied Materials & Interfaces,* **6**, 7665 (2014)

4. Hyesung Cho, Sang Moon Kim, Yun Sik Kang, Junsoo Kim, Segeun Jang, Minhyoung Kim, Hyunchul Park, Jung Won Bang, Soonmin Seo, Kahp-Yang Suh, Yung-Eun Sung and Mansoo Choi, "Multiplex lithography for multilevel multiscale architectures and its application to polymer electrolyte membrane fuel cell", *Nature Communications,* **6**, 9984 (2015)

5. Dong Young Chung, Kyung Jae Lee Seung-Ho Yu, Minhyoung Kim, Stanfield Youngwon Lee, Ok-Hee Kim, Hyung-Jin Park and Yung-Eun

Sung, "Alveoli-Inspired Facile Transport Structure of N-Doped Porous Carbon for Electro-chemical Energy Applications". *Advanced Energy Materials*, **5**, 1401309 (2015).

6. Yun Sik Kang, Kwang-Hyun Choi, Docheon Ahn, Myeong Jae Lee, Jaeyoon Baik, Dong Young Chung, Mi-Ju Kim, Stanfield Youngwon Lee, **Minhyoung Kim**, Heejong Shin, Kug-Seung Lee, Yung-Eun Sung, "Effect of post heat-treatment of composition-controlled PdFe nanoparticles for oxygen reduction reaction", *Journal of Power Sources,* **303**, 234 (2016)

7. Sang Moon Kim, Yun Sik Kang, Chiyeong Ahn, Segeun Jang, **Minhyoung Kim**, Yung-Eun Sung, Sung Jong Yoo, Mansoo Choi, "Prism-patterned Nafion membrane for enhanced water transport in polymer electrolyte membrane fuel cell", Journal of Power Sources, **317**, 19 (2016)

8. Dong Young Chung, Myeong Jae Lee, **Minhyoung Kim**, Heejong Shin, Mi-Ju Kim, Ji Mun Yoo, Subin Park, Yung-Eun Sung, "CO electro-oxidation reaction on Pt nanoparticles: understanding peak multiplicity through thiol derivative molecule adsorption", Catalysis Today, in press